Research Paper

GEOSPHERE

GEOSPHERE, v. 15, no. 6

https://doi.org/10.1130/GES02013.1

11 figures; 3 tables

CORRESPONDENCE:
caroline.heineke@uni-muenster.de

CITATION: Heineke, C., Hetzel, R., Nilius, N.-P., Glotzbach, C., Akal, C., Christl, M., and Hampel, A., 2019, Spatial patterns of erosion and landscape evolution in a bivergent metamorphic core complex revealed by cosmogenic ^{10}Be: The central Menderes Massif (western Turkey): Geosphere, v. 15, no. 6, p. 1846–1868, https://doi.org/10.1130/GES02013.1.

Science Editors: Raymond M. Russo, Shanaka de Silva
Associate Editor: Jeff Lee

Received 25 May 2018
Revision received 25 May 2019
Accepted 23 July 2019

Published online 30 September 2019

Spatial patterns of erosion and landscape evolution in a bivergent metamorphic core complex revealed by cosmogenic ^{10}Be: The central Menderes Massif (western Turkey)

Caroline Heineke[1,*], Ralf Hetzel[1,*], Nils-Peter Nilius[2,*], Christoph Glotzbach[3,*], Cüneyt Akal[4,*], Marcus Christl[5,*], and Andrea Hampel[2,*]

[1]Institut für Geologie und Paläontologie, Westfälische Wilhelms-Universität Münster, Corrensstraße 24, D-48149 Münster, Germany
[2]Institut für Geologie, Leibniz Universität Hannover, Callinstraße 30, D-30167 Hannover, Germany
[3]Institut für Geologie und Geodynamik, Universität Tübingen, Wilhelmstraße 56, D-72074 Tübingen, Germany
[4]Dokuz Eylül University, Engineering Faculty, Department of Geological Engineering, Tınaztepe Campus, Buca, TR-35160 Izmir, Turkey
[5]Laboratory of Ion Beam Physics, ETH Zurich, Otto-Stern-Weg 5, HPK G23, 8093 Zurich, Switzerland

ABSTRACT

In extensional provinces with low-angle normal faulting (such as the Aegean region), both tectonic processes and erosion induce landscape change, but their interaction during the evolution of topography and relief accompanying continental extension has rarely been addressed. Here we present local and catchment-wide ^{10}Be erosion rates that document the spatial pattern of erosion in the central Menderes Massif, a metamorphic core complex consisting of two asymmetric mountain ranges (Bozdağ and Aydın) bound by detachment faults and active grabens. Catchment-wide erosion rates on the northern flank of the Bozdağ Range are rather low (40–110 mm/k.y.) but reach values of >300 mm/k.y. on the steep southern escarpment—a pattern that reflects both topography and bedrock lithology. In the Aydın Range, erosion rates are generally higher, with mean erosion rates of ~190 and ~260 mm/k.y. on the northern and southern flank, respectively, and more variable along strike. In both ranges, erosion rates of ridge crests derived from amalgamated clasts are 30–90 mm/k.y. The difference between local and catchment-wide erosion rates indicates that topographic relief increases in most parts of the massif in response to ongoing fault-related uplift and concomitant river incision. Our findings document that tectonic processes exert a significant control on landscape evolution during active continental extension and are reflected in both the topographic signature and the spatial pattern of erosion. In the Menderes Massif, rock susceptibility to weathering and erosion is a dominant factor that controls the erosional contribution to rock exhumation, which varies spatially between ~10% and ~50%.

INTRODUCTION

In tectonically active regions, tectonic and surface processes act in concert to shape Earth's landscape (e.g., Willett et al., 2006; Bishop, 2007). These processes include the activity of faults, as well as erosion, sediment transport, and deposition and ultimately lead to the exhumation of rocks. In this context, a fundamental difference between regions undergoing crustal shortening or extension exists. While in regions of shortening, rock exhumation occurs exclusively by erosion, in extensional environments, both tectonic denudation (i.e., normal faulting) and erosion contribute to the exhumation of rocks (England and Molnar, 1990; Ring et al., 1999). In regions where extension has been predominantly accommodated by low-angle detachment faulting, tectonic denudation has often been considered to be the dominant mechanism for rock exhumation (e.g., Foster and John, 1999; Ring et al., 1999; Brichau et al., 2008). On the other hand, erosional denudation exerts an important control on rock exhumation and landscape evolution in mountains bounded by high-angle normal faults (e.g., Harbor, 1997; Armstrong et al., 2003). In such ranges, ^{10}Be-based erosion rates tend to be higher at the center of faults and lower near their tips, although the rates often vary considerably along strike (e.g., Densmore et al., 2009; Stock et al., 2009; Rossi et al., 2017; Roda-Boluda et al., 2019). In contrast to mountains bounded by high-angle normal faults, rates of erosion and the concomitant development of topography and relief have rarely been quantified in regions with low-angle detachment faults (Reinhardt et al., 2007a; Buscher et al., 2013).

In the Aegean extensional province, extension and detachment faulting led to the exhumation of metamorphic rocks from mid-crustal levels in several metamorphic massifs (e.g., the Rhodope massif, the Attic-Cycladic massif, and the Menderes Massif; Fig. 1) (e.g., Gautier et al., 1993; Hetzel et al., 1995a; Grasemann et al., 2012; Jolivet et al., 2013). In this connection, the Menderes Massif in western Turkey was recognized as the first example of bivergent extension, i.e., the exhumation of rocks occurred along two detachments faults with opposite sense of shear (Gessner et al., 2001). This finding and the fact that the Menderes Massif is entirely located above sea level render it ideally suited to investigate the interplay between tectonic and surface processes and their relative contribution to exhumation in an extensional environment. So far, the contribution of erosion to rock exhumation has only been investigated along a narrow transect through the central part of the Menderes Massif by combining ^{10}Be catchment-wide erosion rates with low-temperature thermochronology

*E-mails: caroline.heineke@uni-muenster.de; rahetzel@uni-muenster.de; nilius@geowi.uni-hannover.de; christoph.glotzbach@uni-tuebingen.de; cuneyt.akal@deu.edu.tr; mchristl@phys.ethz.ch; hampel@geowi.uni-hannover.de

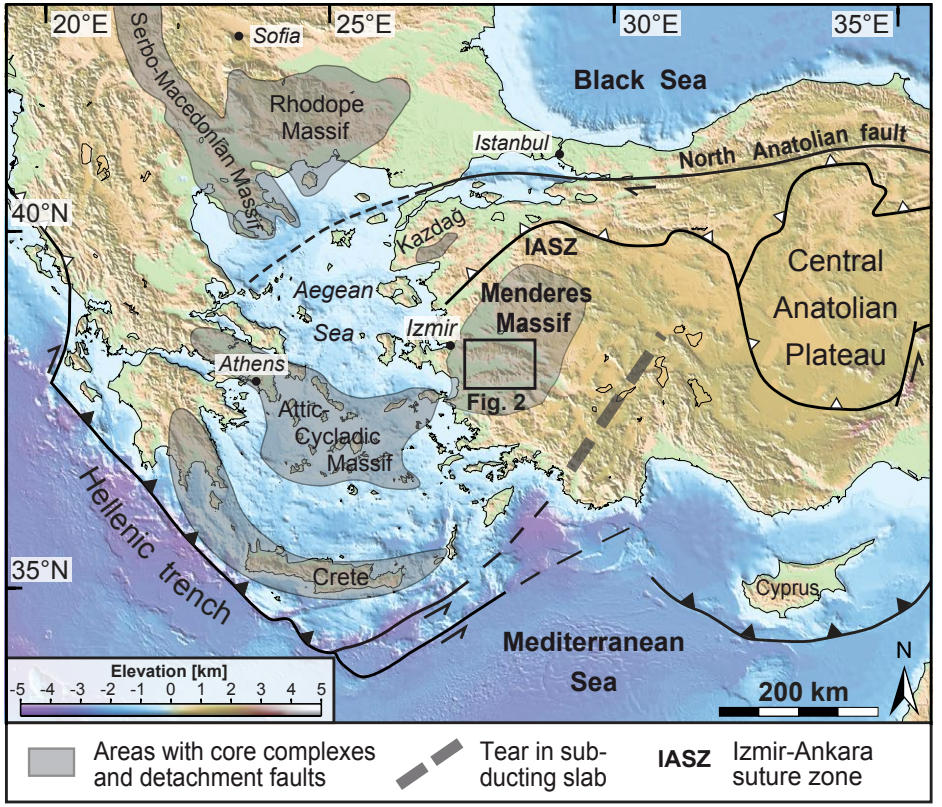

Figure 1. Map of the Eastern Mediterranean region showing the Menderes Massif and other metamorphic massifs with detachment faults (modified from Oner and Dilek, 2011).

(Buscher et al., 2013; Wölfler et al., 2017). However, to what extent erosion varies across the entire central Menderes Massif and how ongoing crustal extension and erosional denudation control the landscape evolution of the massif is still largely unknown.

Cosmogenic nuclides enable the quantification of erosion rates on local and catchment scales in various geological settings (e.g., Brown et al., 1995; Small et al., 1997; Hancock and Kirwan, 2007; Meyer et al., 2010; Portenga and Bierman, 2011). Furthermore, the combination of spatially averaged, catchment-wide erosion rates with local rates of erosion at the outcrop scale can place constraints on the development of topography and local relief (Meyer et al., 2010; Wolff et al., 2018). Combined with digital elevation data, cosmogenic nuclide-derived erosion rates can further be used to deduce the erosional pattern of entire mountain ranges and thus aid the identification of processes that drive landscape evolution on various spatial scales. In this context, the development of new geomorphologic tools to analyze the dynamic state of river networks, river profiles, and drainage divide motion as well as the relationships between topographic parameters and erosion have proven highly valuable in identifying tectonic processes that shape Earth's surface (e.g., DiBiase et al., 2010; Kirby and Whipple, 2012; Perron and Royden, 2013; Willett et al., 2014).

Here, we present local ^{10}Be erosion rates for 14 ridge crests and spatially averaged erosion rates for 31 catchments in the central Menderes Massif to resolve the spatial pattern of erosion across the massif. These data allow us to draw conclusions on the development of local relief during the ongoing extension and—in combination with the analysis of river networks—enable us to infer processes that have shaped the morphology of the central Menderes Massif during continental extension.

GEOLOGICAL SETTING

The Aegean region and western Turkey are located in the backarc of the Hellenic subduction zone (Fig. 1) and, during the past 25 m.y., have experienced

pronounced extension caused by the progressive rollback of the subducting African plate (e.g., Jolivet and Faccenna, 2000; Brun and Sokoutis, 2010; Jolivet et al., 2013). The extensional deformation, aided by erosional denudation, led to the exhumation of mid-crustal rocks, which are exposed in several metamorphic massifs in Greece, Bulgaria, and western Turkey (Fig. 1). GPS data show that extension in this entire region is still ongoing (Reilinger et al., 2010). At present, western Turkey—with the Menderes Massif in its central part—is extending at a rate of ~20 mm/yr in a north-south direction (Aktuğ et al., 2009).

The Menderes Massif consists of three submassifs, which are separated by two major east-west–striking grabens—the Gediz Graben and the Büyük Menderes Graben (e.g., Seyitoğlu and Scott, 1991; Yılmaz et al., 2000; Gürer et al., 2009; Çiftçi and Bozkurt, 2010) (Fig. 2A). The long-lasting history of extension of the Menderes Massif started with a first phase of extension during the late Oligocene and the early Miocene, when the rocks of the northern submassif were largely exhumed by normal faulting (e.g., Işık and Tekeli, 2001; Thomson and Ring, 2006; Ersoy et al., 2010). Subsequently, the metamorphic rocks of the central submassif were exhumed in the footwalls of two low-angle normal faults—the Gediz and Büyük Menderes detachments—which strike east-west and dip to the north and south, respectively (e.g., Hetzel et al., 1995a, 1995b; Emre and Sözbilir, 1997; Bozkurt and Oberhänsli, 2001; Gessner et al., 2001, 2013) (Figs. 2B and 2C). The Gediz detachment operated with a top-to-the-N to NNE shear sense, whereas the shear sense of the Büyük Menderes detachment is top-to-the-S to SSW (Hetzel et al., 1995b; Emre, 1996; Gessner et al., 2001; Işık et al., 2003). Both detachments are cut by the high-angle normal faults of the Gediz and Büyük Menderes grabens, which are seismically active as documented by raised fluvial terraces, fault scarps, and earthquakes (Ambraseys, 1971; Eyidoğan and Jackson, 1985; Altunel, 1999; Çiftçi and Bozkurt, 2010). Sedimentological and stratigraphic data indicate that the transition from low-angle detachment faulting to high-angle normal faulting occurred in the latest Pliocene to early Quaternary (e.g., Purvis and Robertson, 2005; Oner and Dilek, 2011).

The central Menderes Massif comprises two mountain ranges, the Bozdağ and the Aydın range, which are separated by the Küçük Menderes Graben (Fig. 2A). Both mountain ranges are characterized by a topographic asymmetry with rather steep mountain flanks facing the Küçük Menderes Graben and shallow-dipping flanks on the sides of the two detachment faults (Fig. 2B). The Gediz detachment along the northern side of the Bozdağ Range is exceptionally well preserved owing to highly resistant cataclasites with a thickness of 20–50 m and the widespread presence of quartz-rich mylonites underneath (Hetzel et al., 1995b; Emre, 1996; Buscher et al., 2013). Therefore, streams incising the Gediz detachment form narrow valleys with steep hillslopes (Figs. 3A and 3B). The Büyük Menderes detachment along the southern flank of the Aydın Range is less well preserved, because the cataclasites associated with this fault are less than 5 m thick (Emre and Sözbilir, 1997; Hetzel et al., 2013; observations made during fieldwork of this study). In addition, the dominant lithologies underneath this detachment are mica schists and phyllites, which are susceptible to weathering and erosion, while resistant quartzites are absent (Wölfler et al., 2017). As a consequence, most valleys at the Büyük Menderes detachment are broader, yet deeply incised, and exhibit planar hillslopes (Fig. 3C). Apart from the metamorphic rocks, two belts of Neogene sedimentary rocks extend along the northern and southern margin of the central Menderes Massif (Fig. 2A). These strata are well exposed due to footwall uplift and ongoing normal faulting along the main boundary faults of the Gediz and Büyük Menderes grabens.

The metamorphic rocks of the central Menderes Massif constitute a nappe pile that formed during Late Cretaceous to Eocene plate convergence and crustal shortening along the Izmir-Ankara suture zone (e.g., Şengör et al., 1984; Ring et al., 1999; van Hinsbergen et al., 2010; Gessner et al., 2013). The Menderes nappes include, from lowest to highest structural level, the Bayındır, Bozdağ, Çine, and Selimiye nappes, which in turn are overlain by the Cycladic Blueschist Unit in the west (Ring et al., 1999; Gessner et al., 2013) (Figs. 2A and 2C). The Gediz and Büyük Menderes detachments cut obliquely through the nappe pile, and during their activity, slivers of Çine nappe were emplaced as klippen against rocks of the Bayındır nappe in their footwalls (Fig. 2A) (Hetzel et al., 1995b; Buscher et al., 2013; Wölfler et al., 2017). The boundaries of the tectonometamorphic units define an east-west–trending synform, which developed during bivergent north-south extension (Gessner et al., 2001). Together with the detachment faults, this synform appears to control the present-day topography of the submassif and in particular the escarpments facing the Küçük Menderes Graben (Fig. 2C).

The rocks of the Bayındır and Bozdağ nappes constitute the dominant lithological units in the central Menderes Massif. These nappes mainly consist of greenschist- to amphibolite-facies two-mica schists, phyllites, and quartzites, with minor amounts of marble and local amphibolite layers (Dora et al., 1990; Hetzel et al., 1998; Candan et al., 2011). In contrast, the structurally higher Çine and Selimiye nappes are made up of orthogneisses, pelitic gneisses, as well as minor amounts of metapelites and granites (e.g., Hetzel and Reischmann, 1996; Hetzel et al., 1998; Ring et al., 1999; Candan et al., 2001). These nappes mainly occur in the eastern part of the submassif near the Küçük Menderes Graben or as tectonic klippen on the two detachment faults (Fig. 2A).

Recent studies that employed low-temperature thermochronology revealed a two-stage history of cooling and detachment faulting for the central Menderes Massif (Gessner et al., 2001; Ring et al., 2003; Buscher et al., 2013; Wölfler et al., 2017; Nilius et al., 2019) (Fig. 2). The first phase occurred in the middle Miocene (ca. 16 to ca. 10 Ma), whereas the second phase lasted from the latest Miocene to the late Pliocene–early Quaternary (ca. 6 to ca. 2 Ma). The second phase was most pronounced in the eastern part of the Bozdağ Range (i.e., in the region south of Salihli town; see Fig. 4) as evident from a phase of rapid slip (~4 mm/yr) along the Gediz detachment between 4 and 2 Ma (Buscher et al., 2013) and Plio-Quaternary cooling ages from detrital apatite fission-track analyses (Asti et al., 2017). This interpretation is consistent with the fact that the highest topography of the entire Menderes Massif occurs in this region and with the observation that the Gediz detachment is particularly well preserved here.

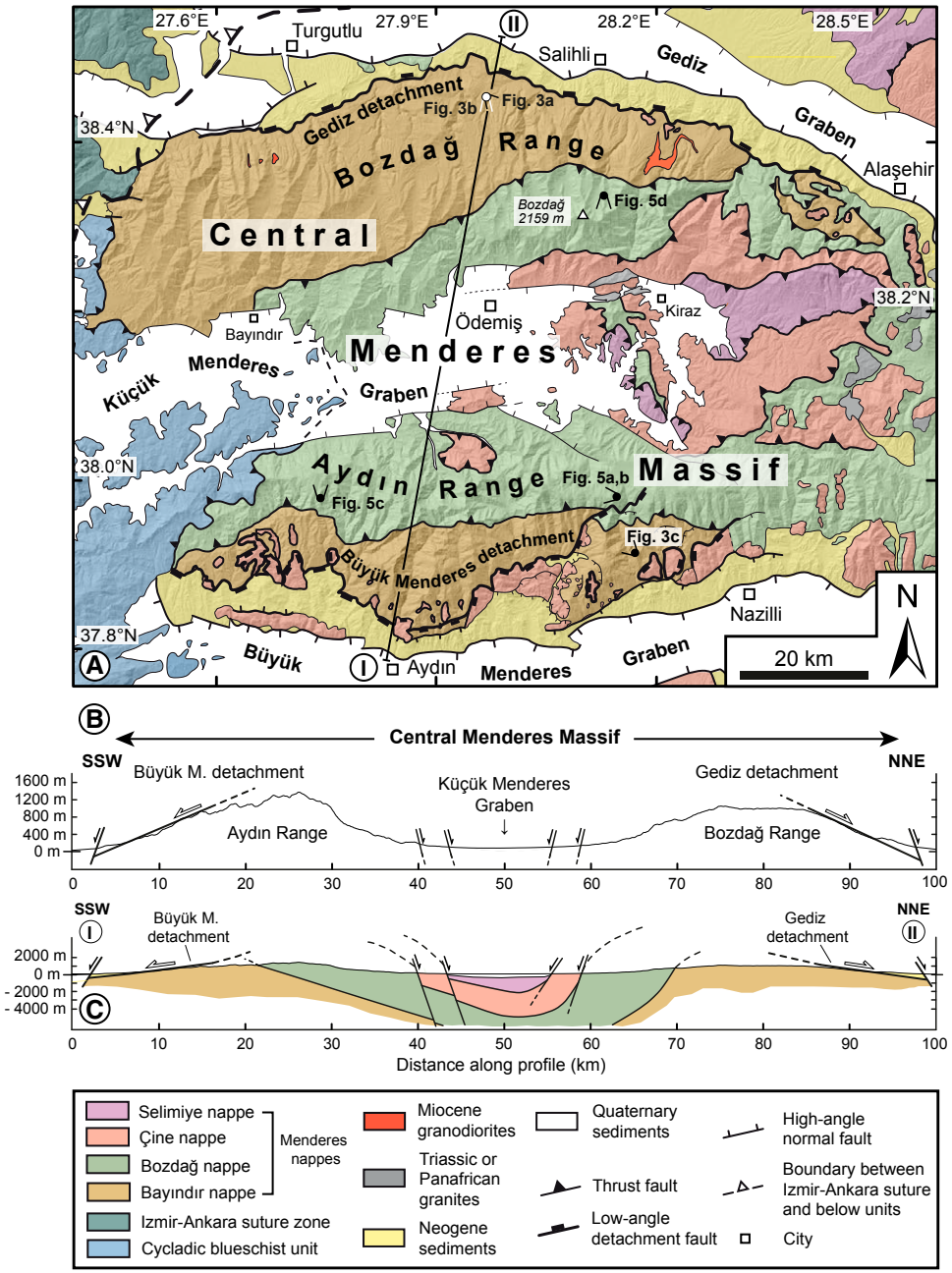

Figure 2. (A) Geological map of the central Menderes Massif (modified from Wölfler et al., 2017, and complemented with observations made during fieldwork of this study). (B) Topographic profile across the central Menderes Massif (vertical exaggeration = 5). Note the topographic asymmetry of the Bozdağ and Aydın mountain ranges with shallow-dipping flanks on the sides of the two detachment faults and steep flanks toward the Küçük Menderes Graben. (C) Geological profile (no vertical exaggeration) showing the Menderes nappe stack, which defines a synform beneath the Küçük Menderes Graben (based on Gessner et al., 2011, and observations made during fieldwork of this study).

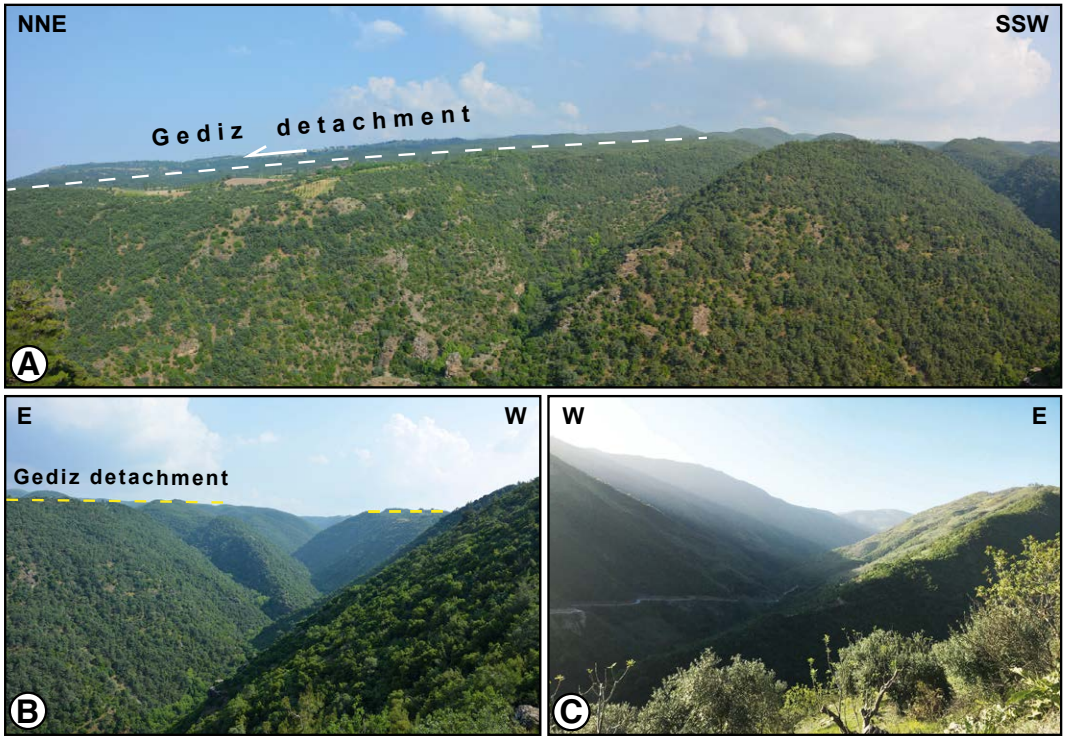

Figure 3. (A) Photograph of the Gediz detachment surface dipping 15° to the north. Rivers have cut through the cataclastic detachment surface, forming steep valleys. (B) Exemplary catchment of the northern slope of the Bozdağ Range (uphill view). Flat-topped mountain crests represent the Gediz detachment. (C) Exemplary catchment of the southern slope of the Aydın Range (upstream view). Valleys exhibit planar hillslopes that are less steep than in the Bozdağ Range.

METHODS

Catchment-Wide and Local Erosion Rates from Cosmogenic ^{10}Be

Cosmogenic nuclides are increasingly used to measure erosion rates over millennial time scales at outcrop or catchment scale (e.g., Cerling and Craig, 1994; Niedermann, 2002; Dunai, 2010; Portenga and Bierman, 2011). The erosion rate E (mm/k.y.) of a steadily eroding bedrock surface is approximately inversely proportional to its cosmogenic nuclide concentration and given by:

$$E = [(P/C) - \lambda]z^*, \quad (1)$$

where P is the local surface production rate in atoms per gram per year (at/g/yr); C is the nuclide concentration at the surface (at/g); λ is the decay constant of the nuclide (1/yr); and z^* is the absorption depth scale (i.e., the effective attenuation length divided by rock density) (Lal, 1991). Owing to the decrease of the production rate with depth, erosion rates calculated from cosmogenic nuclide concentrations are averaged over the time interval needed to erode one absorption depth z^* (i.e., ~60 cm; Granger et al., 1996). Depending on the erosion rate, this time interval typically corresponds to 10^2–10^5 years (e.g., von Blanckenburg, 2006). The relationship given in Equation (1) can be applied to quantify local erosion and to derive spatially averaged erosion rates for entire river catchments by determining the ^{10}Be concentration in quartz of sand samples from active streams (Brown et al., 1995; Bierman and Steig, 1996; Granger et al., 1996). This approach assumes that (1) quartz is homogeneously distributed in the eroding rocks; (2) the sediment in the stream channels is well mixed; (3) erosion in the catchment is in steady state (i.e., nuclide production is equal to the outflux of the nuclide via erosion and radioactive decay); and (4) erosion is uniform through time (e.g., von Blanckenburg, 2006; Granger and Riebe, 2007). We will evaluate the validity of these different assumptions in the discussion.

Sampling Strategy, Sample Preparation, and Calculation of Erosion Rates

For this study, we measured the ^{10}Be concentration of 31 stream sediment samples and 14 samples from ridge crests to derive both catchment-wide and

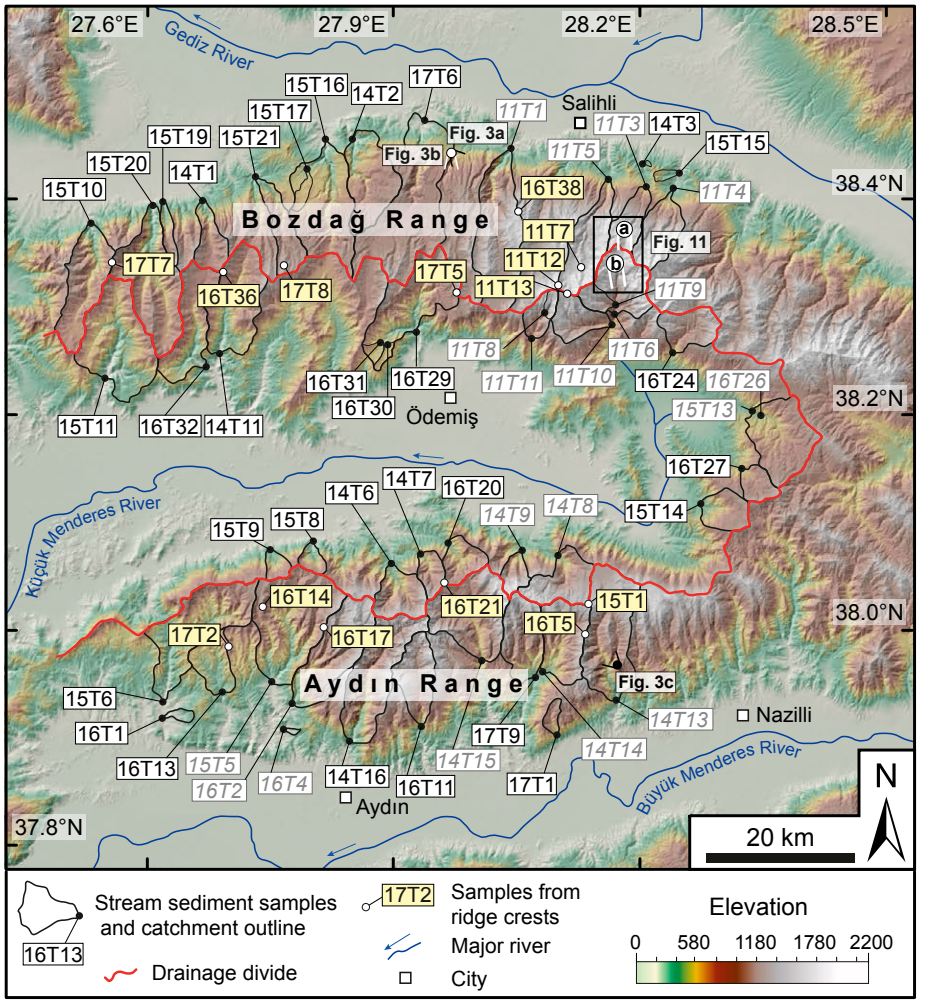

Figure 4. Shaded-relief image of the study area. Sampling sites for ^{10}Be drainage basin erosion rates are labeled with sample numbers in white boxes. Catchment outlines are shown in black. Sample numbers in gray correspond to samples that have previously been published by Buscher et al. (2013), Wölfler et al. (2017), and Heineke et al. (2017) (for details see Table 1). Positions of ridge-crest samples are labeled with sample numbers in yellow boxes.

local erosion rates across the entire central Menderes Massif (Fig. 4). We also include the catchment-wide ^{10}Be erosion rates previously published by Buscher et al. (2013), Wölfler et al. (2017), and Heineke et al. (2017) (Fig. 4, gray sample numbers). We collected our sediment samples along strike of the Bozdağ and Aydın ranges from streams that flow into the Gediz, Küçük Menderes, and Büyük Menderes grabens, respectively. Each sediment sample was taken from several points along the respective stream over a distance of 20–60 m. Most samples are from rivers that exclusively drain metamorphic rocks. Yet, four samples (14T3, 15T15, 16T1, and 16T4) were taken from streams that flow through the Neogene sedimentary rocks exposed along the northern and southern margins of the massif (Fig. 2A). Note that the erosion rate derived from sample 16T4 has been published by Heineke et al. (2017).

To quantify the erosion of ridge crests, we took samples consisting of 1500–2600 bedrock clasts with a length of 1–3.5 cm on 14 mountain crests (Fig. 4). Amalgamated samples of clasts or grus were used previously to quantify local erosion rates and to constrain changes in topographic relief due to river incision (Small et al., 1999; Meyer et al., 2010; Strobl et al., 2012; Wolff et al., 2018). This sampling approach builds on results of previous studies, which

have shown that erosion rates for bedrock outcrops may differ significantly from the actual long-term erosion rate because bedrock erosion mainly occurs by the episodic removal of small blocks or chips (Small et al., 1997, 1999; Anderson, 2002; Reinhardt et al., 2007b; Muzikar, 2008). For example, Small et al. (1997) showed that the apparent bedrock erosion rate determined after removal of a 0.4-m-thick chip deviates from the mean erosion rate by up to +50% or –25%, respectively, depending on the sampling time within the chipping cycle. Model calculations by Reinhardt et al. (2007b) indicate that for a chip thickness of 0.1–0.2 m, ~100 or more samples are needed to reduce the standard error induced by the sampling to <1%. For these reasons, amalgamated clast samples are well suited to obtain accurate long-term erosion rates at the outcrop scale (e.g., Small et al., 1999; Meyer et al., 2010).

We apply the approach of amalgamating clasts to ridge crests in the Bozdağ and Aydın mountain ranges, which generally exhibit smooth, convex profiles and vary in width from a few to several tens of meters (Fig. 5). Commonly, the crests are sparsely vegetated with grass, shrubs, or small trees, and the surface is covered by an up to 10-cm-thick soil or regolith layer containing variable amounts of bedrock clasts (Fig. 5B). Intervening patches of bedrock outcrop occur either as bedrock knobs, sticking out from the surroundings by a few decimeters (Fig. 5C), or are nearly flush with the surface (Fig. 5D). We collected the clasts for all amalgamated samples from the thin soil or regolith on the highest, subhorizontal part of the ridge crests but avoided bedrock outcrops and quartz clasts derived from resistant quartz veins (Fig. 5D). We did not sample cultivated ridges, ridge crests with fire lanes (which occur in the western Bozdağ Range), and sites where wind mills have been constructed (Fig. 5A). The clasts for each sample were taken over distances of 40–100 m to obtain representative erosion rates over a length of several tens of meters along each crest. Depending on crest width, this procedure resulted in sampling areas of ~200 to ~1000 m^2 and 1500–2600 clasts per sample (i.e., two to seven clasts per square meter). Although fewer clasts may have been sufficient to calculate erosion rates, we argue that a larger clast number increases the probability of obtaining a representative erosion rate as explained above (cf. Small et al., 1997; Reinhardt et al., 2007b).

The chemical separation of Be from the amalgamated clast and stream sediment samples was carried out at the cosmogenic nuclide laboratory of the University of Münster. In a first step, all bedrock clasts from the ridge-crest samples were crushed. Then all samples were sieved and washed. Subsequently, the 250–500 µm grain-size fraction of all samples was split into a magnetic and a non-magnetic fraction using a Frantz magnetic separator. For two samples from ridge crests (16T36 and 16T38), we also used the 125–250 µm grain-size fraction because these samples comprised fine-grained phyllites and contained insufficient quantities of quartz in the coarser fraction. The subsequent chemical leaching procedure consisted of one etching step in 6 M HCl at 80 °C, four subsequent etching steps in dilute HF/HNO_3 in a heated ultrasonic bath (Kohl and Nishiizumi, 1992), and two alternating etching steps in aqua regia and 8 M HF to obtain pure quartz (Goethals et al., 2009). Samples 16T36, 16T38, 17T7, and 17T8 consisted of phyllitic schists and were only etched once in dilute HF/HNO_3 and then treated with fluorosilicic acid (H_2SiF_6, 30%) to enrich quartz. After chemical cleaning of quartz, ~0.3 mg of Be carrier was added to all samples. Following complete dissolution of quartz in HF (40%), the samples were redissolved and converted into chloride form using 6 M HCl. Beryllium was separated using successive anion and cation exchange columns and precipitated as $Be(OH)_2$ at pH 8–9. Following the transformation to BeO at 1000 °C and target preparation for accelerator mass spectrometry (AMS), ^{10}Be was analyzed at the AMS facility "TANDY" of the ETH Zurich (Christl et al., 2013). Local and catchment-wide erosion rates were calculated from the blank-corrected ^{10}Be concentrations with version 2.3 of the CRONUS-Earth online calculator (Balco et al., 2008; http://hess.ess.washington.edu) using the time-invariant production rate scaling model of Lal (1991) and Stone (2000). Note that we did not use a topographic shielding factor for calculating the catchment-wide erosion rates because it was shown recently that this correction is not required (DiBiase, 2018).

River Network Analysis

Normalized Channel Steepness

The evolution of topography is linked to changes in river channels, which produce relief as they erode through rock. In general, graded-river profiles can be described by a power-law relationship between channel slope (S) and the contributing upstream drainage area (A):

$$S = k_s A^{-\theta}, \quad (2)$$

where k_s designates the channel steepness and θ the concavity index (Flint, 1974). This scaling relationship only holds downstream of a critical threshold drainage area (A_{crit}, commonly <5 km^2) over which a transition from colluvial channels to fluvial channels occurs (Montgomery and Foufoula-Georgiou, 1993; Stock and Dietrich, 2003; Wobus et al., 2006). Downstream of this transition, changes in lithology, rock uplift rate, or climate lead to the development of segmented river profiles, whereby each segment can be described by its own steepness and concavity index. At steady state, the concavity index θ is thought to be insensitive to differences in lithology, rock uplift rate, and climate (Kirby and Whipple, 2001; Wobus et al., 2006) and commonly falls in the range of 0.4–0.6 (Snyder et al., 2000; Duvall et al., 2004; Wobus et al., 2006). In contrast, the steepness index k_s varies with these factors, rendering it a suitable metric to resolve landscape response to, for example, rock uplift. Since the steepness of a channel is an effective measure of channel slope, k_s also depends on θ (cf. Sklar and Dietrich, 1998), and a normalization of k_s is required to enable a comparison between streams of different drainage networks. For a reference concavity θ_{ref}, the normalized steepness index k_{sn} is defined as:

$$k_{sn} = S A^{\theta ref} \quad (3)$$

and can be determined for any point in a river network (e.g., Whipple et al., 2017).

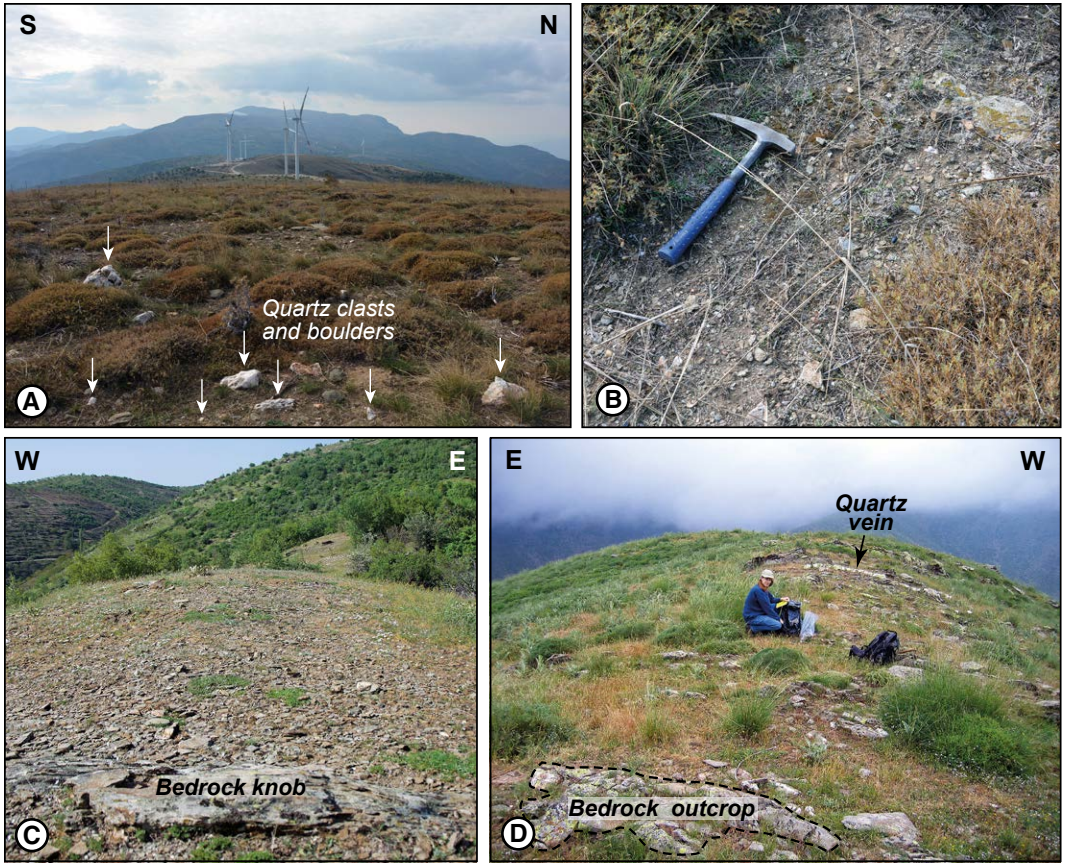

Figure 5. Representative photographs of ridge crests in the central Menderes Massif; we sampled these ridge crests to determine local erosion rates (see Methods section in text for details of sampling approach and Figure 2 for location of the pictures). (A) Broad, 50–70-m-wide ridge crest in the eastern Aydın Range. The size of the area from which we collected sample 15T1 was ~200 m × 50 m. White arrows indicate quartz clasts and boulders derived from quartz veins, which we avoided during sampling. (B) Close-up view of the ridge-crest surface shown in (A) with typical bedrock clasts that were sampled (hammer for scale). Sample 15T1 yielded an erosion rate of 51 ± 5 mm/k.y. (C) Narrow, ~15-m-wide ridge crest in the western Aydın Range where we took sample 16T14 (the size of the sampled area was ~50 m × 10 m). Bedrock knobs such as the one visible in the foreground were avoided during sampling. Sample 16T14 yielded an erosion rate of 87 ± 9 mm/k.y. (D) Narrow, ~8-m-wide ridge crest in the Bozdağ Range, where we collected sample 11T7; size of area was ~40 m × 5 m. Bedrock patches and quartz veins such as those seen in the foreground and background, respectively, were not sampled. Sample 11T7 gave an erosion rate of 70 ± 6 mm/k.y.

In order to derive a suitable reference concavity for streams in the central Menderes Massif, we analyzed chi-elevation plots of the sampled catchments and deduced the respective concavity index for the trunk channel of each catchment (cf. Perron and Royden, 2013). Subsequently, we calculated the mean from all concavity indices, which yielded a reference concavity of 0.4 ± 0.2 (2σ) for the study area. Finally, normalized steepness indices were determined for river segments of 1 km length for streams draining the Bozdağ and Aydın mountain ranges.

Mapping of Chi (χ) Values for Stream Networks

Drainage divides constitute dynamic geomorphic features that migrate (either progressively or by discrete river capture) due to different rates of channel erosion on opposite sides of the divide (Gilbert, 1877; Bishop, 1995; Clark et al., 2004; Bonnet, 2009; Prince et al., 2011; Perron et al., 2012). Hence, the assessment of drainage divide stability and channel equilibrium conditions can serve as a quantitative criterion for the evaluation of landscape (dis) equilibrium and constitutes a valuable tool to infer temporal changes in river networks on various spatial scales.

Streams that originate near a common drainage divide and have the same base level generally experience the same drop of elevation along their course. Yet, if the steady-state elevation profiles of the rivers differ (i.e., the individual profile for which erosion would balance rock uplift), the cross-divide elevation of opposing channel heads will be unequal (Willett et al., 2014). This implies that the drainage divide is unstable and the river network will adjust until a stable divide position is attained. Assessment of steady-state channel elevation throughout the river network can be achieved by mapping the parameter chi

(χ), which serves as a metric for the steady-state elevation of a channel at a location x (Willett et al., 2014). Chi is defined as an integral function of position in the channel network and given by:

$$\chi = \int_{x_b}^{x} \frac{A_0}{A(x')}^{\frac{m}{n}} dx', \quad (4)$$

where x_b and x correspond to the lower (base level) and upper bound (position x in the channel) of the integral, A_0 is an arbitrary scaling area (e.g., 1 km^2), and m and n are parameters whose ratio corresponds to a theoretical intrinsic concavity index (Perron and Royden, 2013). Assuming spatially constant tectonic forcing and homogenous rock properties (i.e., uniform erodibility) along stream, differences in chi across a drainage divide imply disequilibrium conditions and motion of the divide in the direction of higher chi (or higher steady-state channel elevation) to attain equilibrium (Willett et al., 2014).

We generated maps of chi for the central Menderes Massif using TopoToolbox, a MATLAB-based program for the analysis of digital elevation models (Schwanghart and Scherler, 2014). We restricted our analysis to rivers that drain the slopes of the Bozdağ and Aydın mountain ranges, respectively, and did not consider the large streams in the three major grabens.

RESULTS

Erosion Rates from Cosmogenic ^{10}Be

In the Bozdağ Range, catchment-wide erosion rates range from ~40 to ~370 mm/k.y., with distinct differences between the northern and southern flank of the mountain range (Table 1; Figs. 6 and 7). Catchments on the northern range flank mostly erode at rates of ~40–110 mm/k.y., except for two catchments in the central part of the range, which yielded higher rates (Fig. 7A). On the southern flank, high erosion rates of >350 mm/k.y. occur at the steep escarpment south of Bozdağ Mountain and decrease toward the east and west (Fig. 7B). In the Aydın Range, most of the ^{10}Be erosion rates are relatively high (~150 to ~430 mm/k.y.) with considerable variations along strike of the range (Figs. 6, 7C, and 7D). Two small catchments in Neogene sedimentary rocks NW of Aydın town yielded erosion rates of ~84 and ~108 mm/k.y., whereas two similar catchments SE of Salihli erode at higher rates of ~206 and ~331 mm/k.y.

The local ^{10}Be erosion rates for ridge crests fall mainly in the range from ~30 to ~90 mm/k.y. and are similar in the Bozdağ and Aydın mountains (Table 2; Fig. 6). These rates are significantly lower than most catchment-wide erosion rates, with the exception of the western Bozdağ Range, where local and catchment-wide erosion rates are similar. In the Aydın Range, two samples yielded quite different rates of 13 ± 1 and 165 ± 20 mm/k.y., respectively. The low erosion rate of ~13 mm/k.y. for sample 17T2 in the west can be attributed to the resistant bedrock lithology of the sampled crest, which is located in augen gneisses of the Çine nappe. The sample with the rate of ~165 mm/k.y. was taken just above the Büyük Menderes detachment in an area with highly faulted and weathered mica schists, which may explain this rather high rate.

Channel Steepness and Chi (χ) Values in the Stream Network

The spatial pattern of normalized channel steepness for streams that drain the northern slope of the Bozdağ Range reveals particularly steep channels in the eastern part of the mountain range (Fig. 8). These steep channel segments, with k_{sn} values of ≥80, typically stretch over a length of 4–7 km and can be traced along strike of the Gediz detachment, occurring at approximately the same position in adjacent stream networks (Fig. 8). In a westerly direction, the channel steepness decreases, and most trunk channels in the central and western part of the Bozdağ Range have k_{sn} values below 80. On the southern slope of the Bozdağ Range, steep channel segments with k_{sn} values of 80–130 are restricted to the area near Bozdağ peak, whereas farther east and west, channels are generally less steep (Fig. 8). Along the northern slope of the Aydın Range, steep channel segments occur only in the upstream part of rivers that flow into the Küçük Menderes Graben. On the southern slope of the Aydın Range moderately steep channels occur in the center of the mountain range, and k_{sn} values generally decrease to the west and east.

The cross-divide pattern of chi values changes significantly along strike of the Bozdağ Range. In the eastern part of the range, a marked difference in chi values between the northern and southern slope of the mountain range exists (Fig. 9). This difference in chi across the drainage divide disappears in a westerly direction, and in the westernmost part of the Bozdağ Range, chi values of streams are similar on both sides of the drainage divide. In the Aydın Range, the cross-divide differences in chi values are generally less pronounced than in the Bozdağ Range, with streams flowing northward into the Küçük Menderes Graben having lower chi values than streams south of the drainage divide.

DISCUSSION

Our new catchment-wide and local ^{10}Be erosion rates as well as river network analyses show that there are considerable differences in the spatial patterns of erosion in the central Menderes Massif. In the following, we first evaluate the spatially averaged erosion rates for catchments in the Bozdağ and Aydın ranges. In the second section, local erosion rates of ridge crests and the development of topographic relief in the central Menderes Massif are discussed. The imprint of normal faulting on landscape morphology is evaluated in the third section, which also includes a discussion on the distribution of channel steepness and on drainage divide mobility. Finally, we compare our ^{10}Be-based erosion rates with exhumation rates derived from low-temperature thermochronology to estimate the relative importance of erosion and normal faulting on landscape evolution during continental extension.

TABLE 1. ^{10}Be CONCENTRATIONS AND EROSION RATES FOR CATCHMENTS IN THE MENDERES MASSIF, WESTERN TURKEY

Sample†	Location		Sample elevation (m)	Mean catchment elevation (m)	Mean slope (°)	Catchment area (km²)	^{10}Be concentration# (10^4 at/g)	Production rate		**Catchment-wide erosion rate** (mm/k.y.)**	Internal uncertainty** (1σ) (mm/k.y.)	External uncertainty** (1σ) (mm/k.y.)	Time scale†† (k.y.)
	Latitude (°N)	Longitude (°E)						Spallation (at/g/yr)	Muons (at/g/yr)				
Bozdağ Range													
17T6	38.4824	27.9424	175	839	16.0	157	1.93 ± 0.13	7.60	0.100	**300**	21	30	2.1
16T24	38.2639	28.2392	499	1078	21.5	34	5.10 ± 0.25	9.12	0.108	**132**	7	12	4.8
16T29	38.2853	27.9293	220	752	22.1	92	2.68 ± 0.20	7.08	0.097	**202**	15	21	3.2
16T30	38.2722	27.8909	464	585	10.9	4.3	4.77 ± 0.27	6.19	0.092	**100**	6	9	6.4
16T31	38.2738	27.8887	450	587	13.6	5.4	5.91 ± 0.29	6.20	0.092	**80**	4	7	8.0
16T32	38.2516	27.6735	166	690	20.8	65	5.71 ± 0.36	6.73	0.095	**90**	6	9	7.1
15T10	38.3876	27.5345	216	756	21.9	70	8.36 ± 0.43	7.11	0.097	**64**	3	6	10
15T11	38.2397	27.5523	131	575	20.1	112	8.75 ± 0.44	6.14	0.092	**53**	3	5	12
15T15	38.4343	28.2457	213	425	22.1	3.4	1.49 ± 0.12	5.44	0.087	**331**	26	35	2.2
15T16	38.4654	27.8197	154	707	16.0	104	4.77 ± 0.29	6.85	0.096	**109**	7	10	5.9
15T17	38.4371	27.7967	417	606	9.4	6.8	5.70 ± 0.31	6.31	0.093	**85**	5	8	7.5
15T19	38.4069	27.6234	226	781	25.5	12	5.59 ± 0.31	7.25	0.098	**98**	5	9	6.5
15T20	38.4033	27.6104	195	749	24.2	104	9.96 ± 0.50	7.07	0.097	**53**	3	5	12
15T21	38.4303	27.7355	244	869	21.7	36	6.26 ± 0.31	7.78	0.101	**93**	5	8	6.9
14T1	38.4087	27.6700	236	819	22.4	28	13.68 ± 0.63	7.41	0.099	**40**	2	4	16
14T2	38.4677	27.8534	177	746	17.1	69	2.42 ± 0.22	7.06	0.097	**223**	21	27	2.9
14T3	38.4425	28.2032	269	400	24.7	0.5	2.34 ± 0.14	5.32	0.086	**206**	12	19	3.5
14T11	38.2636	27.6912	174	706	21.1	84	4.79 ± 0.29	6.79	0.096	**108**	7	10	5.9
11T1*	38.4580	28.0447	190	1081	21.5	104	9.66 ± 0.42	9.17	0.108	**69**	3	6	9.3
11T3*	38.4205	28.2074	565	1356	18.6	28	11.36 ± 0.59	11.27	0.118	**71**	4	7	9.0
11T4*	38.4182	28.2389	295	1355	24.9	42	5.43 ± 0.29	11.26	0.118	**150**	8	14	4.3
11T5*	38.4286	28.1610	375	1455	24.7	59	12.19 ± 0.42	12.12	0.122	**71**	2	6	9.0
11T6*	38.3012	28.1693	645	1439	28.5	61	3.11 ± 0.20	11.95	0.122	**277**	18	28	2.3
11T8*	38.2990	28.0835	915	1491	32.9	6	2.47 ± 0.19	12.42	0.124	**362**	28	39	1.8
11T9*	38.3076	28.1685	720	1429	28.3	12	5.75 ± 0.51	11.87	0.121	**148**	13	18	4.3
11T10*	38.2889	28.1640	570	1228	27.5	31	2.76 ± 0.30	10.22	0.114	**271**	30	36	2.4
11T11*	38.2781	28.0698	594	1194	27.8	20	1.97 ± 0.18	9.96	0.112	**372**	34	44	1.7
Aydın Range													
17T1	37.9008	28.0987	421	794	22.0	7.3	1.30 ± 0.12	7.27	0.099	**430**	42	52	1.5
17T9	37.9549	28.0703	322	996	26.7	52	3.15 ± 0.19	8.51	0.105	**202**	12	19	3.2
16T1	37.9173	27.6238	131	286	14.3	4.7	5.15 ± 0.36	4.81	0.083	**84**	6	8	8.7
16T2*	37.9299	27.7796	204	1024	25.8	84	3.89 ± 0.24	8.69	0.106	**166**	10	16	3.9
16T4*	37.9067	27.7705	173	266	14.7	1.3	3.99 ± 0.25	4.73	0.083	**108**	7	10	6.8
16T11	37.9074	27.9356	320	1106	26.1	46	2.81 ± 0.17	9.25	0.109	**243**	15	23	2.6
16T13	37.9400	27.6936	259	515	19.5	35	3.17 ± 0.19	5.82	0.090	**144**	9	13	4.4
16T20	38.0818	27.9687	423	800	24.3	26	2.47 ± 0.22	7.33	0.099	**226**	21	27	2.8
15T5*	37.9487	27.7551	186	750	24.5	127	1.29 ± 0.18	7.03	0.097	**420**	59	66	1.5
15T6	37.9325	27.6229	153	594	23.1	102	1.49 ± 0.15	6.21	0.092	**326**	34	41	2.0
15T8	38.0855	27.8043	187	644	25.4	11	3.09 ± 0.39	6.47	0.094	**162**	21	24	4.0
15T9	38.0770	27.7514	260	706	21.8	11	1.72 ± 0.16	6.80	0.096	**306**	30	37	2.1
14T6	38.0641	27.8996	320	942	26.6	38	2.52 ± 0.17	8.17	0.104	**244**	17	24	2.6
14T7*	38.0732	27.9323	416	885	24.7	18	2.99 ± 0.18	7.84	0.102	**198**	12	19	3.2
14T8*	38.0703	28.0990	398	1124	19.9	47	10.25 ± 0.51	9.43	0.110	**67**	3	6	9.6
14T9*	38.0752	28.0565	402	1105	28.6	15	5.39 ± 0.29	9.24	0.109	**126**	7	12	5.1
14T13*	37.9342	28.1713	232	1011	23.0	103	7.01 ± 0.31	8.61	0.106	**91**	4	8	7.0
14T14*	37.9593	28.0818	359	968	25.3	60	2.05 ± 0.14	8.33	0.105	**305**	22	31	2.1
14T15*	37.9716	28.0102	487	998	25.9	92	4.36 ± 0.22	8.53	0.106	**145**	7	13	4.4
14T16	37.8959	27.8463	199	976	30.7	94	1.52 ± 0.23	8.34	0.105	**413**	63	70	1.5
Eastern Küçük Menderes													
16T26*	38.2062	28.3406	455	839	15.0	81	8.10 ± 0.31	7.57	0.100	**70**	3	6	9.1
16T27	38.1551	28.3211	495	899	16.3	21	6.49 ± 0.39	7.93	0.102	**91**	6	9	7.0
15T13*	38.2075	28.3351	424	834	15.0	83	6.86 ± 0.37	7.54	0.100	**82**	4	8	7.8
15T14	38.1177	28.2724	364	787	16.9	29	4.27 ± 0.28	7.26	0.098	**129**	8	13	5.0

†Samples marked with an asterisk have been published by Buscher et al. (2013), Wölfler et al. (2017), and Heineke et al. (2017).

#Blank-corrected ^{10}Be concentrations. The uncertainty of the ^{10}Be concentration (1σ) includes the error of the blank correction and the propagated error of the analytical uncertainty. The analytical error takes into account the error based on counting statistics, the scatter of the repeated measurement of the same sample, as well as the uncertainty of the standard normalization. ^{10}Be concentrations were measured by accelerator mass spectrometry using the ETH Zurich Tandy system (Kubik and Christl, 2010; Christl et al., 2013). Measured ^{10}Be/^{9}Be ratios are normalized to the secondary standard S2007N with a nominal ^{10}Be/^{9}Be ratio of 28.1×10^{-12} (Kubik and Christl, 2010), considering the ^{10}Be half-life of 1.387 ± 0.012 Ma (Chmeleff et al., 2010; Korschinek et al., 2010). The secondary standard has been calibrated relative to the primary standard ICN 01-5-1 (Nishiizumi et al., 2007; Kubik and Christl, 2010).

**Erosion rates were calculated with the CRONUS-Earth ^{10}Be–^{26}Al online calculator (Balco et al., 2008; http://hess.ess.washington.edu; version 2.3) using the primary calibration data set of Borchers et al. (2016) and the time-invariant production rate scaling model of Lal (1991) and Stone (2000). Note that the erosion rates previously published by Buscher et al. (2013) have been recalculated with this version of the online calculator. For calculating the erosion rates, we used a bedrock density of 2.5 g/cm³ and the mean catchment elevation. For samples 14T3, 15T15, 16T1, and 16T4 from catchments in Neogene sedimentary rocks, a density of 2.2 g/cm³ was used. Internal uncertainties include the analytical uncertainty and the error of the blank correction, whereas external uncertainties also include the systematic uncertainty of the sea-level high-latitude production rate. Note that the 2.7% error (1σ) associated with the ^{10}Be/^{9}Be ratio of the standard S2007N is not included in the uncertainties.

††The time over which erosion rates integrate is calculated by dividing the absorption depth scale of 64 cm and 73 cm for metamorphic rocks and Neogene sediments, respectively, by the erosion rate.

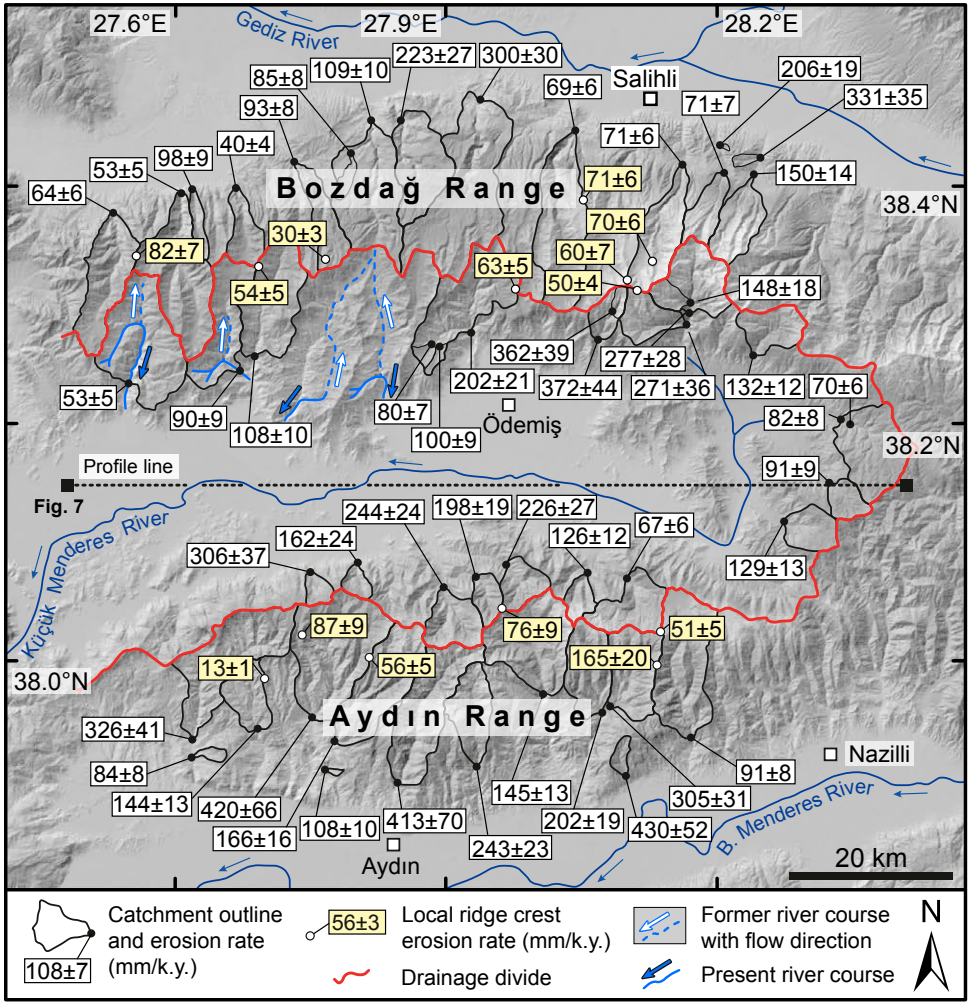

Figure 6. Shaded relief image showing local and catchment-wide erosion rates (mm/k.y.) in the central Menderes Massif (1σ external uncertainties). In the western part of the Bozdağ Range, several rivers have experienced a flow reversal. The former and current river courses are indicated by white and blue arrows, respectively, following Süzen et al. (2006).

Footwall Erosion along the Gediz and Büyük Menderes Detachments

The present-day topography of the central Menderes Massif is the result of a long history of extension, normal faulting, rock uplift, and erosion. The similar structural and topographic asymmetry of the Bozdağ and Aydın mountain ranges is related to their exhumation history in the footwall of the Gediz and Büyük Menderes detachments and the formation of the synform near the Küçük Menderes Graben (Fig. 2). Still, catchment-wide erosion rates in the footwalls of the two detachment faults are markedly different (Fig. 6). We interpret the low erosion rates on the northern slope of the Bozdağ Range to result from the presence of resistant 20–50-m-thick cataclasites and quartz-rich mylonites in the footwall of the Gediz detachment (Hetzel et al., 1995b; Emre, 1996). These rocks protect the detachment from erosion due to their high rock strength (Figs. 3A and 3B). The rather low mean hillslope angles of the respective catchments (16°–25°; Fig. 7A) are an expression of the gently dipping detachment surface. The mean erosion rate for all catchments on the northern mountain slope is 111 ± 22 mm/k.y. (Fig. 7A). Only two catchments in the central portion of the range erode at markedly higher rates of ~223 and

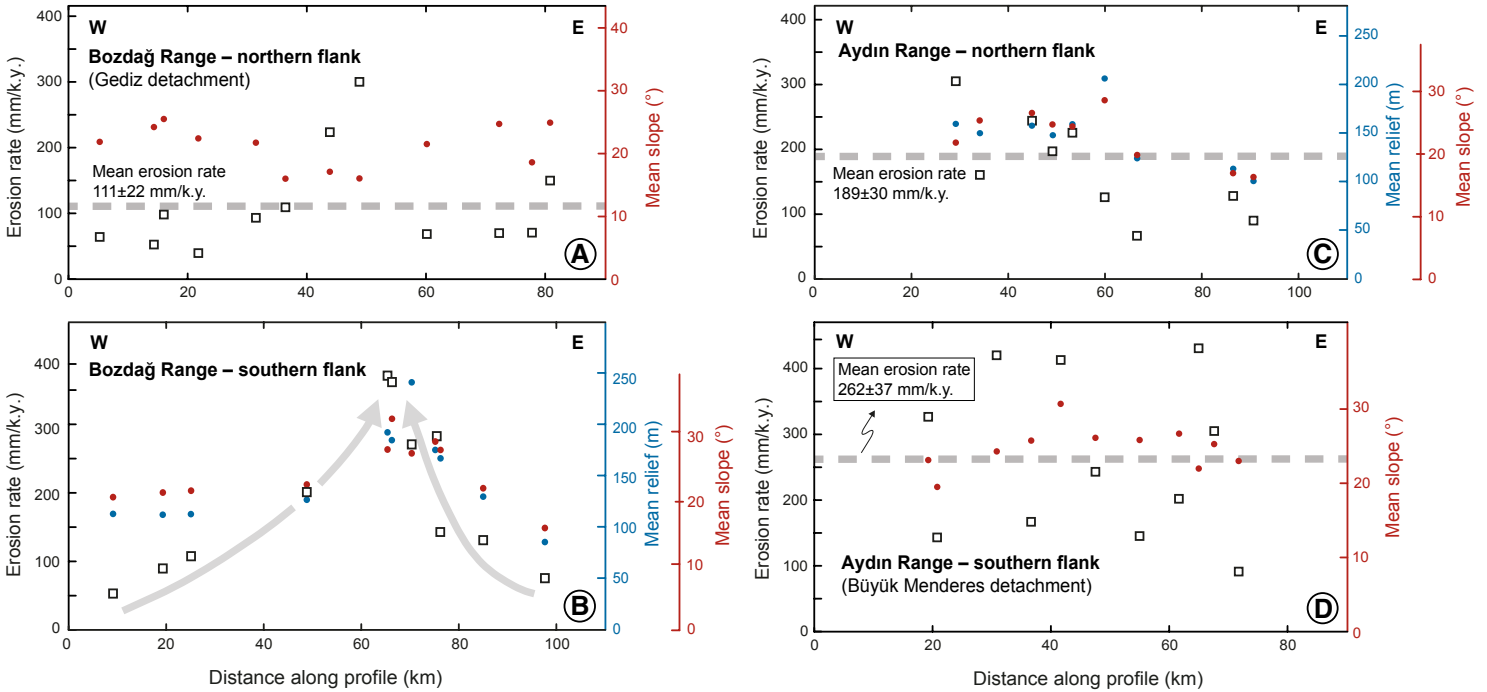

Figure 7. Catchment-wide ^{10}Be erosion rates (open squares) for catchments in the Bozdağ and Aydın mountain ranges plotted against mean relief (blue circles) and mean slope (red circles). The distance between the catchments along the profile corresponds to the distance between the central points of the catchments projected onto the profile line shown in Figure 6. Gray dashed line indicates mean erosion rate of the corresponding mountain range flank. Gray arrows highlight the increase of catchment-wide erosion rates toward the steepest part of the escarpment located south of Bozdağ Mountain. Mean relief was calculated using a moving window with a diameter of 1 km. For further explanation see text. (A) ^{10}Be erosion rates plotted against mean slope for catchments in the footwall of the Gediz detachment (northern flank of Bozdağ Range). (B) ^{10}Be erosion rates for catchments along-strike of the southern flank of the Bozdağ Range plotted against mean catchment relief and mean slope. (C) ^{10}Be erosion rates along northern flank of the Aydın Range plotted against mean catchment relief and mean slope. (D) ^{10}Be erosion rates plotted against mean slope for catchments in the footwall of the Büyük Menderes detachment (southern flank of Aydın Range).

~300 mm/k.y. (Fig. 6). The high erosion rates for these catchments appear to be caused by the presence of weak phyllites and mica schists and the absence of quartz-rich mylonites. Moreover, because the detachment has a very gentle dip in this region, and the catchments are characterized by flat upstream areas, the high erosion rates may mainly reflect the incision of the trunk channels. However, to evaluate this issue in detail, an analysis of drainage basin connectivity would be required, which is beyond the scope of the present study.

In the Aydın Range, catchment-wide erosion rates are quite variable on both sides of the mountain range and—unlike in the Bozdağ Range—do not reflect its topographic asymmetry (Fig. 6). Catchments along the northern flank of the Aydın Range erode at a mean rate of 189 ± 30 mm/k.y., whereas the average erosion rate on the shallower southern slope is 262 ± 37 mm/k.y. (Figs. 7C and 7D). We attribute the rapid erosion of the footwall of the Büyük Menderes detachment (as compared to the Gediz detachment) to be related to the predominance of weak phyllites and mica schists (as opposed to quartz-rich mylonites at the Gediz detachment) and to the thin (<5 m) cataclasites of the detachment (Emre and Sözbilir, 1997; Hetzel et al., 2013; observations made during fieldwork of this study), which do not shield the underlying rocks from erosion. Owing to the susceptibility of the mica schists and phyllites to erosion, the Büyük Menderes detachment is not as well preserved as the Gediz detachment (Wölfler et al., 2017). The considerable along-strike variations in erosion rates for catchments on both sides of the Aydın Range are difficult to explain. In general, such spatial variations may be caused by variations in bedrock quartz content (e.g., Carretier et al., 2015), incomplete mixing of sediment in the catchment, non-uniform erosion through time (e.g., due to the occurrence of debris flows; Kober et al., 2012), or a violation of the steady-state erosion

TABLE 2. ^{10}Be CONCENTRATIONS AND LOCAL EROSION RATES FOR RIDGE CRESTS IN THE CENTRAL MENDERES MASSIF, WESTERN TURKEY

Sample	Location		Sample elevation (m)	Topographic shielding*	^{10}Be concentration† (10^4 at/g)	Production rate		**Local erosion rates§ (mm/k.y.)**	Internal uncertainty§ (1σ) (mm/k.y.)	External uncertainty§ (1σ) (mm/k.y.)	Time scale# (k.y.)
	Latitude (°N)	Longitude (°E)		–		Spallation (at/g/yr)	Muons (at/g/yr)				
Bozdağ Range											
17T8	38.3462	27.7693	1211	1.0	24.03 ± 0.82	10.10	0.113	**30**	1	3	21.3
17T7	38.3497	27.5604	1028	1.0	7.83 ± 0.37	8.78	0.107	**82**	4	7	7.8
17T5	38.3216	27.9790	1193	1.0	11.46 ± 0.45	9.96	0.112	**63**	3	5	10.2
16T38	38.3973	28.0511	1630	1.0	13.60 ± 0.53	13.76	0.129	**71**	3	6	9.0
16T36	38.3406	27.6946	1089	0.9999	12.20 ± 0.75	9.20	0.109	**54**	3	5	11.9
11T7	38.3447	28.1282	1635	1.0	13.85 ± 0.54	13.79	0.129	**70**	3	6	9.1
11T12	38.3269	28.0996	2015	1.0	20.50 ± 1.6	18.00	0.146	**60**	5	7	10.7
11T13	38.3201	28.1096	2090	1.0	25.90 ± 1.0	18.94	0.149	**50**	2	4	12.8
Aydın Range											
17T2	37.9833	27.7009	821	1.0	39.25 ± 0.98	7.44	0.100	**13**	0.4	1	49.2
16T21	38.0449	27.9628	1028	0.9999	8.47 ± 0.74	8.74	0.107	**76**	7	9	8.4
16T17	38.0010	27.8166	1186	0.9998	12.60 ± 0.72	9.84	0.112	**56**	3	5	11.4
16T14	38.0231	27.7427	1023	0.9999	7.37 ± 0.53	8.70	0.106	**87**	6	9	7.4
16T5	37.9942	28.1328	1467	1.0	5.26 ± 0.48	12.13	0.123	**165**	15	20	3.9
15T1	38.0244	28.1366	1495	1.0	16.94 ± 0.88	12.38	0.124	**51**	3	5	12.5

*Topographic shielding was calculated with a 30 m SRTM digital elevation model and the MATLAB script of G. Balco (http://depts.washington.edu/cosmolab/shielding.m).

†Blank-corrected ^{10}Be concentrations. The uncertainty of the ^{10}Be concentration (1σ) includes the error of the blank correction and the propagated error of the analytical uncertainty. The analytical error takes into account the error based on counting statistics, the scatter of the repeated measurement of the same sample, as well as the uncertainty of the standard normalization. ^{10}Be concentrations were measured by accelerator mass spectrometry using the ETH Zurich Tandy system (Kubik and Christl, 2010; Christl et al., 2013). Measured ^{10}Be/^{9}Be ratios are normalized to the secondary standard S2007N with a nominal ^{10}Be/^{9}Be ratio of 28.1×10^{-12} (Kubik and Christl, 2010), considering the ^{10}Be half-life of 1.387 ± 0.012 Ma (Chmeleff et al., 2010; Korschinek et al., 2010). The secondary standard has been calibrated relative to the primary standard ICN 01-5-1 (Nishiizumi et al., 2007; Kubik and Christl, 2010).

§Erosion rates were calculated with the CRONUS-Earth ^{10}Be–^{26}Al online calculator (Balco et al., 2008; http://hess.ess.washington.edu/; version 2.3) using the primary calibration data set of Borchers et al. (2016) and the time-invariant production rate scaling model of Lal (1991) and Stone (2000). For calculating the erosion rates, we used a bedrock density of 2.5 g/cm^3. Internal uncertainties include the analytical uncertainty and the error of the blank correction, whereas external uncertainties also include the systematic uncertainty of the sea-level high-latitude production rate. Note that the 2.7% error (1σ) associated with the ^{10}Be/^{9}Be ratio of the standard S2007N is not included in the uncertainties.

#The time over which erosion rates integrate is calculated by dividing the absorption depth scale of 64 cm by the erosion rate.

assumption (e.g., Heimsath, 2006; Dunai, 2010). Since the quartz content of the phyllites and two-mica schists of the Bozdağ and Bayındır nappes is similar, we argue that variations in the quartz content should have no pronounced effect on the measured ^{10}Be erosion rates in the Aydın Range. With respect to the second assumption of sediment mixing, it should be kept in mind that sediment transport in the channel network of catchments is generally discontinuous (e.g., Benda and Dunne, 1997; Gran and Czuba, 2017). Hence, incomplete sediment mixing in the channels might to some degree explain the observed variability of erosion in the studied catchments. In particular, incomplete sediment mixing is more likely in smaller catchments than in larger ones (Niemi et al., 2005; Delunel et al., 2013), because dispersion and overlap of sediment pulses from several sediment sources is more efficient in larger catchments (Benda and Dunne, 1997). Although our approach of taking a sample from several points along each stream should increase the probability of obtaining a well-mixed sample with a ^{10}Be concentration reflecting the average catchment erosion, we cannot rule out incomplete sediment mixing in our catchments. Regarding the assumptions of uniform erosion through time and a steady state between ^{10}Be production in the catchment and ^{10}Be outflux via sediment export and radioactive decay, it can be expected that these conditions are not fully met in natural settings (Dunai, 2010), and this may apply also to the Aydın Range. The steady state between ^{10}Be influx and outflux may, for example, be violated by a long-term storage of sediments within catchments, even though the absence of fluvial terraces suggests that this process does not play a significant role in our study area (see Fig. 3). According to Heineke et al. (2017), debris flows seem to have no pronounced effect on measured erosion rates in the central Menderes Massif. Thus, it seems at least unlikely that they are the main factor causing the observed variability in catchment erosion. Although the ultimate reasons for this variability remain unclear, we consider it most likely that the observed ^{10}Be erosion rates result from a combination of the different factors described above.

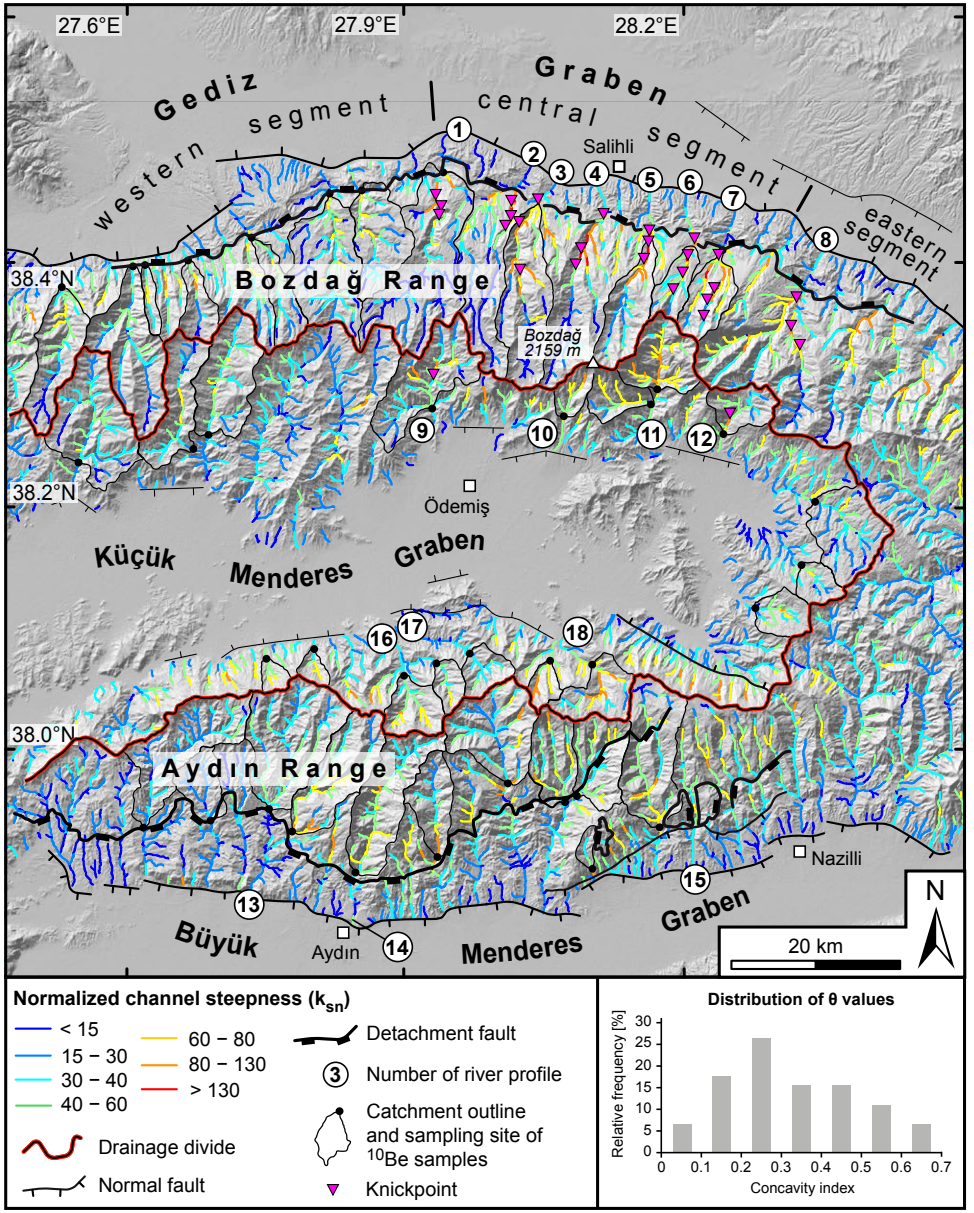

Figure 8. Map of the central Menderes Massif showing the normalized channel steepness of streams. The steepness indices (k_{sn}) were determined for 1-km-long river segments, an upstream area of >1 km², and a reference concavity (θ) of 0.4 ± 0.2 (2σ). The reference concavity corresponds to the mean of the concavity indices calculated for the trunk channels of all sampled catchments (for distribution, see inset figure). The drainage divide of the Küçük Menderes Graben is delineated as red-black line. Knickpoints of streams are only indicated in the area around Bozdağ Mountain and marked by triangles. Numbers in white circles correspond to river profiles shown in Figure 10. The three segments of the high-angle normal fault along the Gediz Graben are indicated.

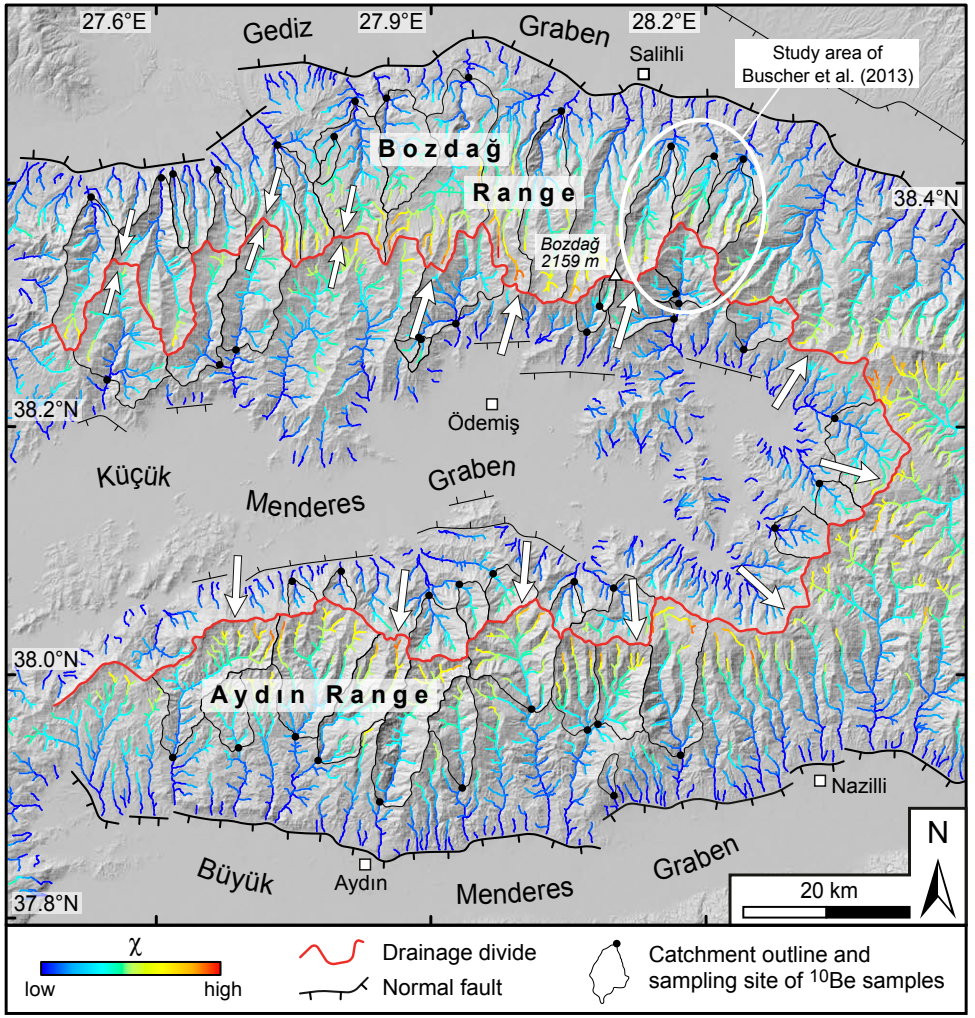

Figure 9. Map of chi (χ) values for streams in the central Menderes Massif. Chi values were calculated for a scaling area A_0 of 1 km² and an m/n ratio of 0.4. Catchment outlines and sampling sites are indicated as black lines and dots, respectively (only catchments in metamorphic rocks are indicated). The drainage divide of the Küçük Menderes Graben is highlighted in red. White arrows indicate whether the divide is migrating (one arrow) or stable (two arrows). White ellipse marks study area of Buscher et al. (2013).

Ridge Crest Erosion and Topographic Relief

Most of our local ^{10}Be erosion rates for ridge crests (i.e., 11 out of 14 values) fall in the narrow interval between 50 ± 4 and 87 ± 9 mm/k.y. (Table 2; Fig. 6), which is considerably smaller than the spread of the catchment-wide erosion rates (Fig. 7). The consistency of the local erosion rates across the massif shows that the amalgamation of a large number of clasts (≥1500) yields robust and representative erosion rates. Hence, this approach can overcome the problem that local erosion rates derived from bedrock outcrops may underestimate or overestimate rates of ridge-crest erosion (cf. Small et al., 1999; Reinhardt et al., 2007b; Meyer et al., 2010; Strobl et al., 2012). The different sampling sites lie at elevations between ~800 and ~2100 meters above sea level (masl) (Table 2); yet despite this significant spread, there is no relation between sample elevation and erosion rate. In addition, the lowering rate of ridge crest appears to be largely independent from crest width, because the broadest of all sampled ridges erodes at a rate of 51 ± 5 mm/k.y. (Fig. 5A),

which is similar to the erosion rate of 70 ± 6 mm/k.y. for the narrowest of all sampled crests (Fig. 5D).

The erosion rates for ridge crests are in most cases lower than the rates obtained for neighboring catchments, indicating that topographic relief in most parts of the central Menderes Massif is growing. Under the assumption that incision rates of rivers are similar to rates of basin erosion, the rate of relief growth equals the difference between local and catchment-wide erosion rates (Meyer et al., 2010). In the Aydın Range, the average erosion rate of 18 catchments is ~230 mm/k.y., whereas rates on intervening ridges are between 13 ± 1 and 87 ± 9 mm/k.y. (except for one high value of ~165 mm/k.y., which we neglect for reasons explained above). Although there is a significant spread in both data sets, we attempt to provide a crude estimate for the rate of relief growth by using average values for local and catchment-wide erosion. We assign an uncertainty of ±100 mm/k.y. to the average value of 230 mm/k.y. for the catchments in the Aydın Range, because this leads to a range of 130–330 mm/k.y., which encompasses the erosion rates obtained for most catchments (14 out of 18). We use a value of 50 ± 30 mm/k.y. as the average rate of ridge-crest lowering. The difference between the two rates is 180 ± 100 mm/k.y., which we interpret as a reasonable estimate for the rate of relief production in the Aydın Range.

In the Bozdağ Range, we consider the western and eastern part of the range separately. In the west, local and catchment-wide erosion rates are almost similar (i.e., 30–82 mm/k.y. versus 40–109 mm/k.y., respectively; Fig. 6). This similarity suggests that local relief in this part of the range does not significantly change, which implies that rock uplift and river incision rates match each other. On the northern flank of the eastern Bozdağ Range, the situation appears to be the same at first sight, because catchment erosion rates in the vicinity of Salihli are similar to rates of ridge-crest lowering (Fig. 6). However, the assumption that river incision rates are similar to spatially averaged erosion rates is unlikely to be correct in this region, because incision of the deep valleys is presumably faster than erosion of the relict Gediz detachment surface that is preserved between the valleys (Figs. 3A and 3B). This interpretation is supported by the observation that the north-flowing rivers incising into the detachment have high channel steepness indices (Fig. 8) and are not graded (Fig. 10A). As a consequence, we argue that—in contrast to the western Bozdağ Range—local relief in the eastern part of the range is increasing, although we do not attempt to provide an estimate for the rate at which topographic relief is growing.

Imprint of Normal Faulting on Landscape Morphology

Normal faulting and rock uplift control the current morphology of the central Menderes Massif and are reflected in the spatial pattern of normalized channel steepness and chi values in the drainage network. In the Bozdağ Range, channel segments with high k_{sn} values of >80 and locally >130 are restricted to the northeastern part of the range (i.e., region near Salihli; Fig. 8, river profiles 2–8), where the Pliocene phase of detachment faulting was most pronounced (Buscher et al., 2013; Asti et al., 2017) and caused the development of knickpoints, which can be traced along-strike of the mountain slope (Figs. 8 and 10A). Another reason for the occurrence of knickpoints in this part of the Bozdağ Range is the formation of the southern boundary fault of the Gediz Graben in the early Quaternary and the subsequent linkage of its three different fault segments (Fig. 8), which may have caused an acceleration in fault throw rates and a relative base-level fall (Kent et al., 2016a). As a consequence, the knickpoints and steep channel segments can be interpreted as a response to sustained tectonic activity and normal faulting since ca. 6 Ma. On the southern flank of the Bozdağ Range, no comparable pattern of steep channel gradients and knickpoints exists, and stream channels are generally less steep and, in most cases, graded (Figs. 8 and 10A). This finding is in accordance with less active, high-angle normal faults in the Küçük Menderes Graben as compared to the Gediz Graben (Rojay et al., 2005).

As outlined above, the exhumation of the Bozdağ Range was accomplished by the Pliocene phase of detachment faulting, which gradually merged into high-angle normal faulting and the development of the Gediz Graben (Çiftçi and Bozkurt, 2010; Oner and Dilek, 2011; Buscher et al., 2013; Kent et al., 2016a). Hence, extension and normal faulting occurred more or less continuously in prolonged phases and were accompanied by river incision and the formation of steep valleys with knickpoints (Fig. 10A). Owing to the resistance of the cataclasites and mylonites of the Gediz detachment to weathering and erosion, the detachment surface is still quite well preserved between the steep valleys (Fig. 3). Thus, the landscape of northeastern Bozdağ Range has not yet fully responded to the base-level fall by ongoing normal faulting.

In the eastern Bozdağ Range, the drainage divide is located near the crest of the steep escarpment south of Bozdağ Mountain (i.e., rather close to the Küçük Menderes Graben; Fig. 4). This position of the divide is somewhat unexpected, because fault-related rock uplift should currently be most pronounced in the vicinity of the active boundary fault of the Gediz Graben, and therefore, one could expect the main divide to be located farther north. We argue that the present position of the drainage divide has been inherited from the pronounced second phase of detachment faulting. During this phase of top-to-the-NNE shearing, the eastern Bozdağ Range was exhumed in the footwall of the Gediz detachment, which shifted the drainage divide far to the south. The spatial pattern of chi values for the stream network reveals marked cross-divide differences in this region, suggesting that the drainage divide is currently migrating back to the north (Fig. 9), despite ongoing normal faulting on the high-angle faults of the Gediz Graben. The inference of a northward-migrating divide is in agreement with our catchment-wide erosion rates, which are high on the steep escarpment south of Bozdağ Mountain and much lower on the northern slope of the mountain range (Fig. 6). Hence, catchments in the south are growing at the expense of catchments north of the divide (Fig. 9). This process of divide migration has advanced most in the area east of Bozdağ Mountain. Here, the northward shift of the divide has removed the entire upstream part of the catchment north of the divide (Fig. 11A) and enlarged the deeply incised southern catchment (Fig. 11B).

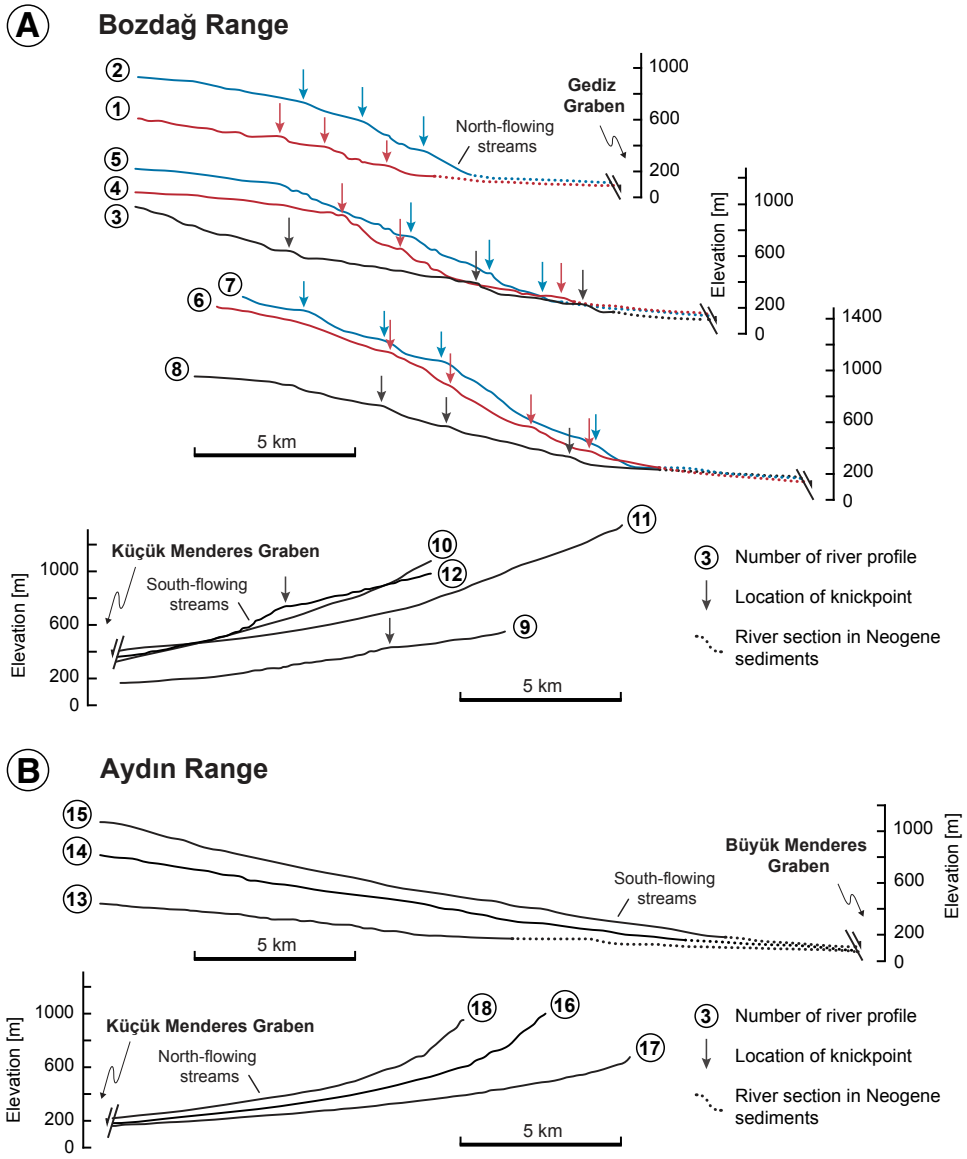

Figure 10. River profiles of streams in bedrock draining (A) the Bozdağ Range and (B) the Aydın Range. Profiles of north-flowing streams on the Bozdağ Range are shown in color only for reasons of clarity. Knickpoints are indicated with arrows. For location of streams, see Figure 8. Vertical exaggeration is 4.

In a westerly direction along the Bozdağ Range, the drainage divide is located in a more central position within the range, and cross-divide differences in chi decrease, suggesting that the drainage divide is stable (Fig. 9). This is supported by the similarity of catchment-wide erosion rates, which are of the same order of ~50–100 mm/k.y. on both sides of the range (Fig. 6). Hence, the process of drainage divide migration to the north as response to faulting and rock uplift appears to be more or less completed in the western Bozdağ Range. Two reasons may be responsible for this. First, the Pliocene phase of detachment faulting was particularly rapid in the eastern part of the detachment (near Salihli, Fig. 9; Buscher et al., 2013) but less pronounced in the west, and second, the western segment of the Gediz Graben boundary fault has slipped at a lower rate than the central and eastern segments in the Quaternary (i.e., ~0.9 mm/yr versus ~1.4 mm/yr in the past ~2 m.y.; Fig. 8) (Kent et al., 2016b). Further evidence for an already accomplished northward shift of the drainage divide is provided by the bifurcation of valleys formed by streams that experienced flow reversal due to divide migration (Süzen et al., 2006) (Fig. 6). Before the northward shift of the divide, the point of confluence of the streams was located north of the drainage divide, whereas it is located south of main divide today. In summary, the spatial pattern of chi values in the Bozdağ Range indicates that the eastern and western parts of the mountain range are in different dynamic states: a quasi-equilibrium state in the west and a transient state in the east. Thus, the eastern part of the range evolves toward the state that has already been reached in western portion of the range.

In the Aydın Range, knickpoints are largely absent, and the river profiles of bedrock channels are graded on both sides of the mountains (Fig. 10B). Isolated steeper channel segments with k_{sn} values >80 are restricted to the proximity of the Büyük Menderes detachment or correlate with high-angle normal faults (Fig. 8). The absence of knickpoints and the lack of very steep channel segments may create the impression that the Aydın Range has been subjected to a lower rate of base-level fall than the Bozdağ Range. However, the similar morphology and elevation of both mountain ranges and the intervening grabens (Fig. 2), the occurrence of surface-rupturing earthquakes along both the Gediz and Büyük Menderes grabens (Altunel, 1999; Ambraseys, 1971), and the presence of uplifted fluvial terraces in their footwalls indicate that the tectonic activity in both ranges is comparable. Therefore, we interpret the river profiles in the Aydın Range to indicate that channel incision and catchment erosion are able to keep pace with the uplift caused by normal faulting. The presence of soft phyllites of the Bayındır nappe and their susceptibility to weathering and erosion can explain why bedrock channels in the Aydın Range are graded and less steep than in the Bozdağ Range.

Similar to the Gediz detachment, faulting on the Büyük Menderes detachment has shifted the drainage divide to a position near the Küçük Menderes Graben (i.e., away from the detachment fault). The pattern of chi values in the Aydın Range indicates that the drainage divide is currently mobile and tends to migrate in a southward direction (Fig. 9). However, cross-divide differences in chi values are generally less pronounced than in the Bozdağ Range and not so clearly correlated with catchment-wide erosion rates, because not all catchments having low chi values exhibit higher erosion rates—as expected if these catchments would act as aggressors and gain area (e.g., catchment 14T6 versus 14T16). In this connection, ongoing uplift of the Aydın Range and river incision in response to normal faulting along the Büyük Menderes Graben may force the drainage divide to remain close to the Küçük Menderes Graben, while the streams flowing into the Küçük Menderes Graben are unable to cause a re-migration of the divide to the south.

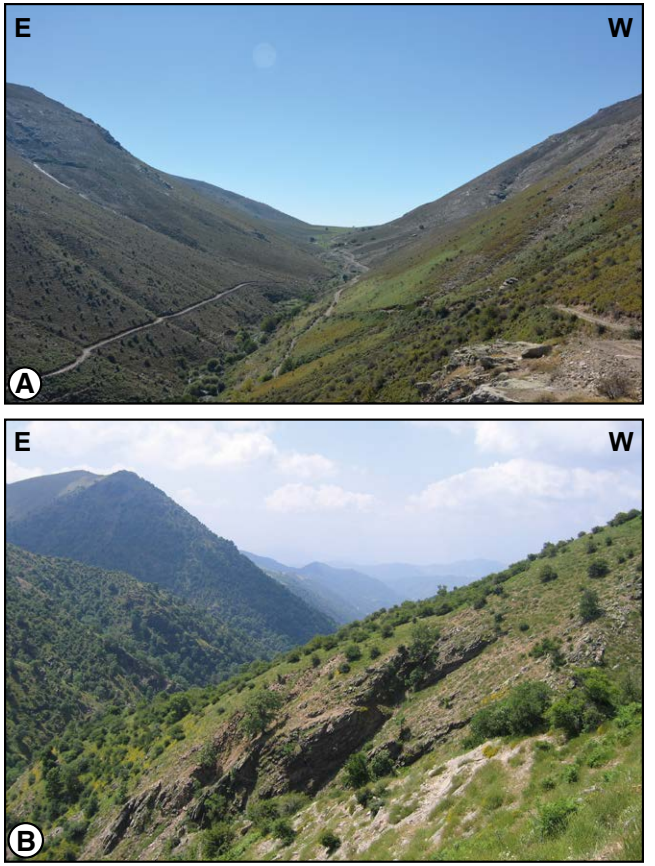

Figure 11. Field photographs in the eastern Bozdağ Range where the northward migration of the drainage divide is most advanced. Positions of viewpoints are indicated in Figure 4. (A) Upstream view in catchment of sample 11T3; catchment drains north into the Gediz Graben. The entire headwater area of this catchment has been removed by enlargement of the aggressor catchment shown in (B). (B) Downstream view in aggressor catchment south side of the drainage divide, where sample 11T6 was taken. Note steep hillslopes and rough topography compared to (A).

Landscape Evolution during Continental Extension

In regions of active continental extension, rock exhumation occurs by a combination of erosional and tectonic denudation. The relative importance of these processes can be evaluated by combining ^{10}Be erosion rates with low-temperature thermochronological data, which provide information on the total exhumation rate. However, only few fault-bounded mountain ranges exist worldwide, where both data on exhumation and erosion rates are available (Reinhardt et al., 2007a; Densmore et al., 2009; Stock et al., 2009). Our study area in the Menderes Massif represents the first example of a metamorphic core complex, for which exhumation and erosion rates have been determined both across and along strike of the fault footwalls. In the following, we will first evaluate the relative importance of erosion and tectonic denudation in the central Menderes Massif. Although such a comparison between erosion and exhumation rates was conducted previously along a narrow transect (Buscher et al., 2013; Wölfler et al., 2017), our new ^{10}Be data set and recently published thermochronological data (Nilius et al., 2019) allow for an improved analysis. Subsequently, we compare our results with data from other normal fault-bounded mountain ranges.

To compare our spatially averaged ^{10}Be erosion rates (Figs. 6 and 7) with exhumation rates derived from thermochronological data in different parts of the central Menderes Massif, we summarize the range of these values in Table 3. In the northern Bozdağ Range, erosion rates in the footwall of the eastern and western Gediz detachment are 70–150 and 40–110 m/m.y., respectively, whereas thermochronological data indicate much higher exhumation rates of 600–1100 m/m.y. and 600–1000 m/m.y. (Gessner et al., 2001; Glodny and Hetzel, 2007; Buscher et al., 2013). Hence, the erosional contribution to rock exhumation at the Gediz detachment is only ~10% (i.e., ~13% in the east versus ~9% in the west; Table 3). In the southern Bozdağ Range, the catchments on the steep escarpment facing the Küçük Menderes Graben erode at rates between 130 and 370 m/m.y. Here, the exhumation rates from thermochronology are lower than at the Gediz detachment (i.e., 300–700 m/m.y.), and thus the relative contribution of erosion to exhumation is ~50% (Table 3). A similar value is obtained for the northern part of the Aydın Range, which forms the opposite margin of the Küçük Menderes Graben. In the footwall of the Büyük Menderes detachment, exhumation rates are slightly lower than at the Gediz detachment (i.e., 400–800 m/m.y.; Wölfler et al., 2017; Nilius et al., 2019). Given the rather high ^{10}Be erosion rates in the southern Aydın Range, erosion is responsible for ~40% of the rock exhumation, although it should be kept in mind that the data variability is large (i.e., 90–430 m/m.y.; Fig. 7D). In summary, the contribution of erosion to rock exhumation was higher at the Büyük Menderes detachment than at the Gediz detachment, where tectonic denudation was the dominant exhumation mechanism (Table 3). Along the high-angle normal faults on both sides of the Küçük Menderes Graben, erosion contributed ~50% to rock exhumation.

A low contribution of erosion to the total denudation as observed for the Gediz detachment was reported from the Rio Torrente catchment in the Spanish Sierra Nevada (Reinhardt et al., 2007a). At this site, apatite fission-track ages indicate total denudation rates between 400 and 1500 m/m.y. over the past 3–4 m.y., whereas an average ^{10}Be-based erosion rate of 44 ± 15 m/m.y. has been determined in the upper part of the catchment, which is characterized by low relief. In the uplands, most of the unroofing hence occurred by low-angle normal faulting (Reinhardt et al., 2007a). The lower parts of the Rio Torrente catchment are affected by high-angle normal faults, which cause footwall uplift and relative base-level fall. Hence, the lower part of the catchment experiences enhanced river incision and hillslope erosion, which results in a much higher ^{10}Be erosion rate of 1600 ± 400 m/m.y. According to Reinhardt et al. (2007a), the difference in the erosion rates indicates that faulting-related changes in base level are not transmitted to the low-relief upland areas. In contrast to the Rio Torrente site, the north-draining catchments in the Bozdağ Range show quite consistently low erosion rates along strike of the Gediz detachment (except for two catchments with easily erodible bedrock, as explained above). This might suggest that uplift and base-level changes due to high-angle normal

TABLE 3. CONTRIBUTION OF EROSION TO EXHUMATION OF THE CENTRAL MENDERES METAMORPHIC CORE COMPLEX

	^{10}Be-based erosion rate (m/m.y.)	Exhumation rate from thermochronology (m/m.y.)	Thermochronometer*	Erosional contribution§ (%)
Northern Bozdağ Range				
Eastern Gediz detachment	70–150	600–1100#	AFT, AHe	**13** (7–19)
Western Gediz detachment	40–110	600–1000†	Ar/Ar biotite	**9** (5–14)
Southern Bozdağ Range (eastern part)	130–370	300–700#	ZHe, AFT, AHe	**50** (19–81)
Northern Aydın Range	70–250	200–400**	AFT, AHe	**53** (18–88)
Southern Aydın Range				
Büyük Menderes detachment	90–430	400–800**	AFT, AHe	**43** (13–70)

*ZHe—zircon (U-Th)/He; AFT—apatite fission track; AHe—apatite (U-Th)/He.
§Values are calculated from mean exhumation and erosion rates (the full range is given in parentheses).
#Buscher et al. (2013).
†Glodny and Hetzel (2007).
**Wölfler et al. (2017); Nilius et al. (2019).

faulting along the Gediz Graben have so far not significantly increased the catchment-wide erosion rates in the footwall of the Gediz detachment. In contrast, faulting-related uplift and base-level changes may have a greater effect in the southern Aydın Range, where erosion rates are higher than in the northern Bozdağ Range (Table 3). However, it should be kept in mind that the presence of different bedrock lithologies also exerts a significant control on catchment erosion and its spatial variability.

In contrast to the Gediz and Büyük Menderes detachment faults, erosion tends to play a larger role in exhuming rocks in the footwall of the high-angle normal faults bounding the Küçük Menderes Graben (Table 3). This result can be compared with two sites in the Basin and Range Province, where ^{10}Be erosion rates and exhumation rates were determined for the footwalls of high-angle normal faults. The first site is the central Wasatch Range, for which Stock et al. (2009) reported ^{10}Be erosion rates between 70 and 170 m/m.y. for catchments at the range front. Because the exhumation rates along most of the range front are between 200 and 400 m/m.y. over the past ~5 m.y. (Ehlers et al., 2003; Armstrong et al., 2004), this indicates that erosion provides an average contribution of ~40% (range: 19%–61%) to the total exhumation rate. At the southern Salt Lake City segment, where exhumation rates reach values of 600–800 m/m.y. (Ehlers et al., 2003; Armstrong et al., 2004), erosion contributes less than 30% to exhumation at the range front (Stock et al., 2009). Toward the interior of the Wasatch Range, catchments are steeper and show higher erosion rates with a larger variability (170–790 m/m.y.) (Stock et al., 2009). Hence, in the core of the Wasatch Range, erosion rates may be as high as the exhumation rates. The Wassuk Range is the second site where exhumation rates based on thermochronology and ^{10}Be erosion rates have been determined (Densmore et al., 2009). In the range center, most apatite (U-Th)/He ages yield exhumation rates between 500 and 800 m/m.y., whereas most catchments erode at rates of 100–300 m/m.y. As a result, the contribution of erosion to exhumation is ~30% (range: 14%–48%). At the southern range tip, where erosion and exhumation rates are 86 ± 4 and 300 ± 10 m/m.y., respectively, the contribution of erosion is ~30%.

In summary, the existing data sets on erosion and exhumation rates in regions of continental extension indicate that erosion provides a non-negligible contribution to rock exhumation along both low-angle and high-angle normal faults. Along low-angle normal faults, the erosional contribution may be as low as ~10%, whereas it is generally higher and more variable along high-angle normal faults with values between 30%–70%. It should be kept in mind, however, that there are only a limited number of sites so far where both ^{10}Be and thermochronological data are available on the same spatial scale and that the data show considerable spatial variability, especially the ^{10}Be erosion rates (e.g., Densmore et al., 2009; Stock et al., 2009; this study). As outlined above, the ultimate reasons for the observed variability in erosion rates are often difficult to determine. Despite these uncertainties, comparisons between erosion and exhumation rates provide important insights into the relative contribution of the different processes that control rock exhumation and landscape evolution in regions of continental extension.

CONCLUSIONS

New catchment-wide erosion rates and the first local ^{10}Be erosion rates for ridge crests in the central Menderes Massif document the spatial pattern of erosion in the entire massif during continental extension. Rates of drainage basin erosion in combination with river network analyses reveal that the geomorphic signature of normal faulting is best preserved in the Bozdağ Range. Its preservation in the landscape is related to the resistant lithologies exposed in the footwall of the Gediz detachment, where steep channel segments and knickpoints record ongoing normal faulting and footwall uplift. In the Aydın Range, the geomorphic signal of normal faulting and uplift is less well preserved, because the lithology in the footwall of the Büyük Menderes detachment is characterized by a thin layer of cataclasites and rather weak phyllites and mica schists, which have a low preservation potential due to their high erodibility. The spatial pattern of chi values in the drainage network, the course of the drainage divide, and cross-divide differences in catchment erosion in the central Menderes Massif document that uplift was most pronounced in the northeastern part of the Bozdağ Range. We infer that this part of the mountain range is still in a state of transience, while the western part of the Bozdağ Range has attained a quasi-equilibrium state. By comparing catchment-wide erosion rates with local rates of ridge-crest lowering, we deduce that the topographic relief in the Aydın Range and eastern Bozdağ Range increases due to ongoing uplift along the active normal faults of the Gediz, Küçük Menderes, and Büyük Menderes grabens.

ACKNOWLEDGMENTS

We thank Eric Portenga, Liam Reinhardt, and Associate Editor Jeff Lee for constructive reviews, which significantly improved this paper. We are grateful to A. Niehus, K. Schoppengerd, and P. Gebbeken for their help during the separation of ^{10}Be from quartz and target preparation. V. Rapelius is thanked for inductively coupled plasma–optical emission spectroscopy analysis. This work was funded by the Deutsche Forschungsgemeinschaft (DFG) grants HE 1704/18-1 and GL 724/7-1 provided to R. Hetzel and C. Glotzbach.

REFERENCES CITED

Aktuğ, B., Nocquet, J.M., Cingöz, A., Parsons, B., Erkan, Y., England, P., Lenk, O., Gürdal, M.A., Kilicoglu, A., Akdeniz, H., and Tekgül, A., 2009, Deformation of western Turkey from a combination of permanent and campaign GPS data: Limits to block-like behavior: Journal of Geophysical Research, v. 114, B10404, https://doi.org/10.1029/2008JB006000.

Altunel, E., 1999, Geological and geomorphological observations in relation to the 20 September 1899 Menderes earthquake, western Turkey: Journal of the Geological Society of London, v. 156, no. 2, p. 241–246, https://doi.org/10.1144/gsjgs.156.2.0241.

Ambraseys, N.N., 1971, Value of historical records of earthquakes: Nature, v. 232, no. 5310, p. 375–379, https://doi.org/10.1038/232375a0.

Anderson, R.S., 2002, Modeling the tor-dotted crests, bedrock edges, and parabolic profiles of high alpine surfaces of the Wind River Range, Wyoming: Geomorphology, v. 46, p. 35–58, https://doi.org/10.1016/S0169-555X(02)00053-3.

Armstrong, P.A., Ehlers, T.A., Chapman, D.S., Farley, K.A., and Kamp, P.J.J., 2003, Exhumation of the central Wasatch Mountains, Utah: 1. Patterns and timing of exhumation deduced from low-temperature thermochronology data: Journal of Geophysical Research, v. 108, no. B3, https://doi.org/10.1029/2001JB001708.

Armstrong, P.A., Taylor, A.R., and Ehlers, T.A., 2004, Is the Wasatch fault footwall (Utah, United States) segmented over million-year time scales?: Geology, v. 32, no. 5, p. 385–388, https://doi.org/10.1130/G20421.1.

Asti, R., Malusà, M.G., and Faccenna, C., 2017, Supradetachment basin evolution unraveled by detrital apatite fission track analysis: The Gediz Graben (Menderes Massif, Western Turkey): Basin Research, v. 30, p. 502–521, https://doi.org/10.1111/bre.12262.

Balco, G., Stone, J.O., Lifton, N.A., and Dunai, T.J., 2008, A complete and easily accessible means of calculation surface exposure ages or erosion rates from ^{10}Be and ^{26}Al measurements: Quaternary Geochronology, v. 3, no. 3, p. 174–195, https://doi.org/10.1016/j.quageo.2007.12.001.

Benda, L., and Dunne, T., 1997, Stochastic forcing of sediment routing and storage in channel networks: Water Resources Research, v. 33, no. 12, p. 2865–2880, https://doi.org/10.1029/97WR02387.

Bierman, P., and Steig, E.J., 1996, Estimating rates of denudation using cosmogenic isotope abundances in sediment: Earth Surface Processes and Landforms, v. 21, no. 2, p. 125–139, https://doi.org/10.1002/(SICI)1096-9837(199602)21:2<125::AID-ESP511>3.0.CO;2-8.

Bishop, P., 1995, Drainage rearrangement by river capture, beheading and diversion: Progress in Physical Geography, v. 19, no. 4, p. 449–473, https://doi.org/10.1177/030913339501900402.

Bishop, P., 2007, Long-term landscape evolution: Linking tectonics and surface processes: Earth Surface Processes and Landforms, v. 32, no. 3, p. 329–365, https://doi.org/10.1002/esp.1493.

Bonnet, S., 2009, Shrinking and splitting of drainage basins in orogenic landscapes from the migration of the main drainage divide: Nature Geoscience, v. 2, no. 11, p. 766–771, https://doi.org/10.1038/ngeo666.

Borchers, B., Marrero, S., Balco, G., Caffee, M., Goehring, B., Lifton, N., Nishiizumi, K., Phillips, F., Schaefer, J., and Stone, J., 2016, Geological calibration of spallation production rates in the CRONUS-Earth project: Quaternary Geochronology, v. 31, p. 188–198, https://doi.org/10.1016/j.quageo.2015.01.009.

Bozkurt, E., and Oberhänsli, R., 2001, Menderes Massif (Western Turkey): Structural, metamorphic and magmatic evolution—A synthesis: International Journal of Earth Sciences (Geologische Rundschau), v. 89, no. 4, p. 679–708, https://doi.org/10.1007/s005310000173.

Brichau, S., Ring, U., Carter, A., Bolhar, R., Monié, P., Stockli, D., and Brunel, M., 2008, Timing, slip rate, displacement and cooling history of the Mykonos detachment footwall, Cyclades, Greece, and implications for the opening of the Aegean Sea basin: Journal of the Geological Society of London, v. 165, p. 263–277, https://doi.org/10.1144/0016-76492006-145.

Brown, E.T., Stallard, R.F., Larsen, M.C., Raisbeck, G.M., and Yiou, F., 1995, Denudation rates determined from the accumulation of in situ-produced ^{10}Be in the Luquillo Experimental Forest, Puerto Rico: Earth and Planetary Science Letters, v. 129, no. 1–4, p. 193–202, https://doi.org/10.1016/0012-821X(94)00249-X.

Brun, J.-P., and Sokoutis, D., 2010, 45 m.y. of Aegean crust and mantle flow driven by trench retreat: Geology, v. 38, no. 9, p. 815–818, https://doi.org/10.1130/G30950.1.

Buscher, J.T., Hampel, A., Hetzel, R., Dunkl, I., Glotzbach, C., Struffert, A., Akal, C., and Rätz, M., 2013, Quantifying rates of detachment faulting and erosion in the central Menderes Massif (western Turkey) by thermochronology and cosmogenic ^{10}Be: Journal of the Geological Society of London, v. 170, no. 4, p. 669–683, https://doi.org/10.1144/jgs2012-132.

Candan, O., Dora, O.Ö., Oberhänsli, R., Çetinkaplan, M., Partzsch, J.H., Warkus, F.C., and Dürr, S., 2001, Pan-African high-pressure metamorphism in the Precambrian basement of the Menderes Massif, western Anatolia, Turkey: International Journal of Earth Sciences (Geologische Rundschau), v. 89, no. 4, p. 793–811, https://doi.org/10.1007/s005310000097.

Candan, O., Oberhänsli, R., Dora, O.Ö., Çetinkaplan, M., Koralay, E., Rimmelé, G., Chen, F., and Akal, C., 2011, Polymetamorphic evolution of the Pan-African basement and Palaeozoic–Early Tertiary Cover Series of the Menderes Massif: Bulletin of the Mineral Research and Exploration, v. 142, p. 121–163.

Carretier, S., Regard, V., Vasallo, R., Martinod, J., Christophoul, F., Gayer, E., Audin, L., and Lagane, C., 2015, A note on ^{10}Be-derived mean erosion rates in catchments with heterogeneous lithology: Examples from the western Central Andes: Earth Surface Processes and Landforms, v. 40, p. 1719–1729, https://doi.org/10.1002/esp.3748.

Cerling, T.E., and Craig, H., 1994, Geomorphology and in-situ cosmogenic isotopes: Annual Review of Earth and Planetary Sciences, v. 22, no. 1, p. 273–317, https://doi.org/10.1146/annurev.ea.22.050194.001421.

Chmeleff, J., von Blanckenburg, F., Kossert, K., and Jakob, D., 2010, Determination of the ^{10}Be half-life by multicollector ICP-MS and liquid scintillation counting: Nuclear Instruments & Methods in Physics Research. Section B, Beam Interactions with Materials and Atoms, v. 268, no. 2, p. 192–199, https://doi.org/10.1016/j.nimb.2009.09.012.

Christl, M., Vockenhuber, C., Kubik, P.W., Wacker, L., Lachner, J., Alfimov, V., and Synal, H.-A., 2013, The ETH Zurich AMS facilities: Performance parameters and reference materials: Nuclear Instruments & Methods in Physics Research. Section B, Beam Interactions with Materials and Atoms, v. 294, no. 7–8, p. 29–38, https://doi.org/10.1016/j.nimb.2012.03.004.

Çiftçi, N.B., and Bozkurt, E., 2010, Structural evolution of the Gediz Graben, SW Turkey: Temporal and spatial variation of the graben basin: Basin Research, v. 22, no. 6, p. 846–873.

Clark, M.K., Schoenbohm, L.M., Royden, L.H., Whipple, K.X., Burchfiel, B.C., Zhang, X., Tang, W., Wang, E., and Chen, L., 2004, Surface uplift, tectonics, and erosion of eastern Tibet from large-scale drainage patterns: Tectonics, v. 23, no. 1, TC1006, https://doi.org/10.1029/2002TC001402.

Delunel, R., van der Beek, P.A., Bourlès, D.L., Carcaillet, J., and Schlunegger, F., 2013, Transient sediment supply in a high-altitude Alpine environment evidenced through a ^{10}Be budget of the Etages catchment (French Western Alps): Earth Surface Processes and Landforms, v. 39, no. 7, p. 890–899, https://doi.org/10.1002/esp.3494.

Densmore, A.L., Hetzel, R., Ivy-Ochs, S., Krugh, W.C., Dawers, N., and Kubik, P.W., 2009, Spatial variations in catchment-averaged denudation rates from normal fault footwalls: Geology, v. 37, p. 1139–1142, https://doi.org/10.1130/G30164A.1.

DiBiase, R.A., 2018, Increasing vertical attenuation length of cosmogenic nuclide production on steep slopes negates topographic shielding corrections for catchment erosion rates: Earth Surface Dynamics: Discussions, v. 6, p. 923–931.

DiBiase, R.A., Whipple, K.X., Heimsath, A.M., and Ouimet, W.B., 2010, Landscape form and millennial erosion rates in the San Gabriel Mountains, CA: Earth and Planetary Science Letters, v. 289, no. 1–2, p. 134–144, https://doi.org/10.1016/j.epsl.2009.10.036.

Dora, O.Ö., Kun, N., and Candan, O., 1990, Metamorphic history and geotectonic evolution of the Menderes massif, *in* Proceedings of International Earth Sciences Congress on Aegean Region, Izmir/Turkey 2, p. 102–115.

Dunai, T.J., 2010, Cosmogenic Nuclides—Principles, Concepts and Applications in the Earth Surface Sciences: Cambridge, UK, Cambridge University Press, 187 p., https://doi.org/10.1017/CBO9780511804519.

Duvall, A., Kirby, E., and Burbank, D.W., 2004, Tectonic and lithologic controls on bedrock channel profiles and processes in coastal California: Journal of Geophysical Research. Earth Surface, v. 109, no. F3, F03002, https://doi.org/10.1029/2003JF000086.

Ehlers, T.A., Willett, S.D., Armstrong, P.A., and Chapman, D.S., 2003, Exhumation of the central Wasatch Mountains, Utah: 2. Thermokinematic model of exhumation, erosion, and thermochronometer interpretation: Journal of Geophysical Research, v. 108, no. B3, p. 2173, https://doi.org/10.1029/2001JB001723.

Emre, T., 1996, The tectonic evolution of the Gediz graben: Geological Bulletin of Turkey, v. 39, p. 1–18.

Emre, T., and Sözbilir, H., 1997, Field evidence for metamorphic core complex, detachment faulting and accommodation faults in the Gediz and Büyük Menderes grabens, Western Anatolia: International Earth Sciences Colloquium on the Aegean and Surrounding Regions, Proceedings, v. 1, p. 73–94.

England, P., and Molnar, P., 1990, Surface uplift, uplift of rocks, and exhumation of rocks: Geology, v. 18, no. 12, p. 1173–1177, https://doi.org/10.1130/0091-7613(1990)018<1173:SUUORA>2.3.CO;2.

Ersoy, Y.E., Helvacı, C., and Sözbilir, H., 2010, Tectono-stratigraphic evolution of the NE- SW-trending superimposed Selendi basin: Implications for late Cenozoic crustal extension in Western Anatolia, Turkey: Tectonophysics, v. 488, no. 1, p. 210–232, https://doi.org/10.1016/j.tecto.2010.01.007.

Eyidoğan, H., and Jackson, J., 1985, A seismological study of normal faulting in the Demirci, Alaşehir and Gediz earthquakes of 1969–70 in western Turkey: Implications for the nature and geometry of deformation in the continental crust: Geophysical Journal International, v. 81, no. 3, p. 569–607, https://doi.org/10.1111/j.1365-246X.1985.tb06423.x.

Flint, J.J., 1974, Stream gradient as a function of order, magnitude, and discharge: Water Resources Research, v. 10, no. 5, p. 969–973, https://doi.org/10.1029/WR010i005p00969.

Foster, D.A., and John, B.E., 1999, Quantifying tectonic exhumation in an extensional orogen with thermochronology: Examples from the southern Basin and Range Province, *in* Ring, U., Brandon, M.T., Lister, G.S., and Willett, S.D., eds., Exhumation Processes: Normal Faulting, Ductile Flow, and Erosion: Geological Society of London Special Publication 154, p. 343–364, https://doi.org/10.1144/GSL.SP.1999.154.01.16.

Gautier, P., Brun, J.-P., and Jolivet, L., 1993, Structure and kinematics of Upper Cenozoic extensional detachment on Naxos and Paros (Cyclades Islands, Greece): Tectonics, v. 12, no. 5, p. 1180–1194, https://doi.org/10.1029/93TC01131.

Gessner, K., Ring, U., Johnson, C., Hetzel, R., Passchier, C.W., and Güngör, T., 2001, An active bivergent rolling-hinge detachment system: Central Menderes metamorphic core complex in western Turkey: Geology, v. 29, no. 7, p. 611–614, https://doi.org/10.1130/0091-7613(2001)029<0611:AABRHD>2.0.CO;2.

Gessner, K., Ring, U., and Güngör, T., 2011, Field Guide to Samos and the Menderes Massif: Along-Strike Variations in the Mediterranean Tethyan Orogen: Geological Society of America Field Guide 23, 52 p., https://doi.org/10.1130/2011.0023.

Gessner, K., Gallardo, L.A., Markwitz, V., Ring, U., and Thomson, S.N., 2013, What caused the denudation of the Menderes Massif: Review of crustal evolution, lithosphere structure, and dynamic topography on southwest Turkey: Gondwana Research, v. 24, no. 1, p. 243–274, https://doi.org/10.1016/j.gr.2013.01.005.

Gilbert, G.K., 1877, Report on the Geology of the Henry Mountains: Washington, D.C., Government Printing Office (U.S. Geographical and Geological Survey of the Rocky Mountain Region), 160 p., https://doi.org/10.3133/70039916.

Glodny, J., and Hetzel, R., 2007, Precise U-Pb ages of syn-extensional Miocene intrusions in the central Menderes Massif, western Turkey: Geological Magazine, v. 144, no. 2, p. 235–246, https://doi.org/10.1017/S0016756806003025.

Goethals, M.M., Hetzel, R., Niedermann, S., Wittmann, H., Fenton, C.R., Kubik, P.W., Christl, M., and von Blanckenburg, F., 2009, An improved experimental determination of cosmogenic $^{10}Be/^{21}Ne$ and $^{26}Al/^{21}Ne$ production ratios in quartz: Earth and Planetary Science Letters, v. 284, no. 1, p. 187–198, https://doi.org/10.1016/j.epsl.2009.04.027.

Gran, K.B., and Czuba, J.A., 2017, Sediment pulse evolution and the role of network structure: Geomorphology, v. 277, p. 17–30, https://doi.org/10.1016/j.geomorph.2015.12.015.

Granger, D.E., and Riebe, C.S., 2007, Cosmogenic nuclides in weathering and erosion, *in* Holland, H.D., and Turekian, K.K., eds., Surface and Ground Water, Weathering, and Soils: Treatise on Geochemistry 5: London, Elsevier, p. 1–43.

Granger, D.E., Kirchner, J.W., and Finkel, R., 1996, Spatially averaged long-term erosion rates measured from in situ produced cosmogenic nuclides in alluvial sediment: The Journal of Geology, v. 104, no. 3, p. 249–257, https://doi.org/10.1086/629823.

Grasemann, B., Schneider, D.A., Stockli, D.F., and Iglseder, C., 2012, Miocene bivergent crustal extension in the Aegean: Evidence from the western Cyclades (Greece): Lithosphere, v. 4, no. 1, p. 23–39, https://doi.org/10.1130/L164.1.

Gürer, Ö.F., Sarıca-Filoreau, N., Özburan, M., Sangu, E., and Doğan, B., 2009, Progressive development of the Büyük Menderes Graben based on new data, western Turkey: Geological Magazine, v. 146, no. 5, p. 652–673, https://doi.org/10.1017/S0016756809006359.

Hancock, G., and Kirwan, M., 2007, Summit erosion rates deduced from ^{10}Be: Implications for relief production in the central Appalachians: Geology, v. 35, no. 1, p. 89–92, https://doi.org/10.1130/G23147A.1.

Harbor, D.J., 1997, Landscape evolution at the margin of the Basin and Range: Geology, v. 25, p. 1111–1114, https://doi.org/10.1130/0091-7613(1997)025<1111:LEATMO>2.3.CO;2.

Heimsath, A.M., 2006, Eroding the land: Steady-state and stochastic rates and processes through a cosmogenic lens, *in* Siame, L.L., Bourlès, D.L., and Brown, E.T., eds., In Situ–Produced Cosmogenic Nuclides and Quantification of Geological Processes: Geological Society of America Special Paper 415, p. 111–129, https://doi.org/10.1130/2006.2415(07).

Heineke, C., Hetzel, R., Akal, C., and Christl, M., 2017, Constraints on water reservoir lifetimes from catchment-wide ^{10}Be erosion rates—A case study from western Turkey: Water Resources Research, v. 53, p. 9206–9224, https://doi.org/10.1002/2017WR020594.

Hetzel, R., and Reischmann, T., 1996, Intrusion age of Pan-African augen gneisses in the southern Menderes Massif and the age of cooling after Alpine ductile extensional deformation: Geological Magazine, v. 133, no. 5, p. 565–572, https://doi.org/10.1017/S0016756800007846.

Hetzel, R., Passchier, C.W., Ring, U., and Dora, O.Ö., 1995a, Bivergent extension in orogenic belts: The Menderes massif (southwestern Turkey): Geology, v. 23, no. 5, p. 455–458, https://doi.org/10.1130/0091-7613(1995)023<0455:BEIOBT>2.3.CO;2.

Hetzel, R., Ring, U., Akal, C., and Troesch, M., 1995b, Miocene NNE-directed extensional unroofing in the Menderes Massif, southwestern Turkey: Journal of the Geological Society of London, v. 152, no. 4, p. 639–654, https://doi.org/10.1144/gsjgs.152.4.0639.

Hetzel, R., Romer, R.L., Candan, O., and Passchier, C.W., 1998, Geology of the Bozdag area, central Menderes Massif, SW Turkey: Pan-African basement and Alpine deformation: International Journal of Earth Sciences (Geologische Rundschau), v. 87, no. 3, p. 394–406.

Hetzel, R., Zwingmann, H., Mulch, A., Gessner, K., Akal, C., Hampel, A., Güngör, T., Petschick, R., Mikes, T., and Wedin, F., 2013, Spatio-temporal evolution of brittle normal faulting and fluid infiltration in detachment fault systems—A case study from the Menderes Massif, western Turkey: Tectonics, v. 32, https://doi.org/10.1002/tect.20031.

Işık, V., and Tekeli, O., 2001, Late orogenic crustal extension in the northern Menderes massif (western Turkey): Evidence for metamorphic core complex formation: International Journal of Earth Sciences (Geologische Rundschau), v. 89, no. 4, p. 757–765, https://doi.org/10.1007/s005310000105.

Işık, V., Seyitoğlu, G., and Çemen, I., 2003, Ductile-brittle transition along the Alaşehir detachment fault and its structural relationship with the Simav detachment fault, Menderes massif, western Turkey: Tectonophysics, v. 374, no. 1, p. 1–18, https://doi.org/10.1016/S0040-1951(03)00275-0.

Jolivet, L., and Faccenna, C., 2000, Mediterranean extension and the Africa-Eurasia collision: Tectonics, v. 19, no. 6, p. 1095–1106, https://doi.org/10.1029/2000TC900018.

Jolivet, L., Faccenna, C., Huet, B., Labrousse, L., Le Pourhiet, L., Lacombe, O., Lecomte, E., Burov, E., Denèle, Y., Brun, J.P., Philippon, M., Paul, A., Salaün, G., Karabulut, H., Piromallo, C., Monié, P., Gueydan, F., Okay, A.I., Oberhänsli, R., Pourteau, A., Augier, R., Gadenne, L., and Driussi, O., 2013, Aegean tectonics: Strain localization, slap tearing and trench retreat: Tectonophysics, v. 597, p. 1–33, https://doi.org/10.1016/j.tecto.2012.06.011.

Kent, E., Boulton, S.J., Whittaker, A.C., Stewart, I.S., and Alçiçek, M.C., 2016a, Normal fault growth and linkage in the Gediz (Alaşehir) Graben, Western Turkey, revealed by transient river long-profiles and slope-break knickpoints: Earth Surface Processes and Landforms, v. 42, no. 5, p. 836–852, https://doi.org/10.1002/esp.4049.

Kent, E., Boulton, S.J., Stewart, I.S., Whittaker, A.C., and Alçiçek, M.C., 2016b, Geomorphic and geological constraints on the active normal faulting of the Gediz (Alaşehir) Graben, Western Turkey: Journal of the Geological Society of London, v. 173, no. 4, p. 666–678, https://doi.org/10.1144/jgs2015-121.

Kirby, E., and Whipple, K.X., 2001, Quantifying differential rock-uplift rates via stream profile analysis: Geology, v. 29, no. 5, p. 415–418, https://doi.org/10.1130/0091-7613(2001)029<0415:QDRURV>2.0.CO;2.

Kirby, E., and Whipple, K.X., 2012, Expression of active tectonics in erosional landscapes: Journal of Structural Geology, v. 44, p. 54–75, https://doi.org/10.1016/j.jsg.2012.07.009.

Kober, F., Hippe, K., Salcher, B., Ivy-Ochs, S., Kubik, P.W., Wacker, L., and Hählen, N., 2012, Debris-flow-dependent variation of cosmogenically derived catchment-wide denudation rates: Geology, v. 40, no. 10, p. 935–938, https://doi.org/10.1130/G33406.1.

Kohl, C.P., and Nishiizumi, K., 1992, Chemical isolation of quartz for measurement of in-situ-produced cosmogenic nuclides: Geochimica et Cosmochimica Acta, v. 56, no. 9, p. 3583–3587, https://doi.org/10.1016/0016-7037(92)90401-4.

Korschinek, G., Bergmaier, A., Faestermann, T., Gerstmann, U.C., Knie, K., Rugel, G., Wallner, A., Dillmann, I., Dollinger, G., Lierse von Gostomski, Ch., Kossert, K., Maiti, M., Poutivtsev, M., and Remmert, A., 2010, A new value for the half-life of ^{10}Be by Heavy-Ion Elastic Recoil Detection and liquid scintillation counting: Nuclear Instruments & Methods in Physics Research. Section B, Beam Interactions with Materials and Atoms, v. 268, no. 2, p. 187–191, https://doi.org/10.1016/j.nimb.2009.09.020.

Kubik, P.W., and Christl, M., 2010, ^{10}Be and ^{26}Al measurements at the Zurich 6 MV Tandem AMS facility: Nuclear Instruments & Methods in Physics Research. Section B, Beam Interactions with Materials and Atoms, v. 268, no. 7, p. 880–883, https://doi.org/10.1016/j.nimb.2009.10.054.

Lal, D., 1991, Cosmic ray labeling of erosion surfaces: In situ nuclide production rates and erosion models: Earth and Planetary Science Letters, v. 104, no. 2–4, p. 424–439, https://doi.org/10.1016/0012-821X(91)90220-C.

Meyer, H., Hetzel, R., Fügenschuh, B., and Strauss, H., 2010, Determining the growth rate of topographic relief using in situ-produced ^{10}Be: A case study in the Black Forest, Germany: Earth and Planetary Science Letters, v. 290, no. 3, p. 391–402, https://doi.org/10.1016/j.epsl.2009.12.034.

Montgomery, D.R., and Foufoula-Georgiou, E., 1993, Channel network source representation using digital elevation models: Water Resources Research, v. 29, no. 12, p. 3925–3934, https://doi.org/10.1029/93WR02463.

Muzikar, P., 2008, Cosmogenic nuclide concentrations in episodically eroding surfaces: Theoretical results: Geomorphology, v. 97, p. 407–413, https://doi.org/10.1016/j.geomorph.2007.08.020.

Niedermann, S., 2002, Cosmic-ray-Produced Noble Gases in Terrestrial Rocks: Dating Tools for Surface Processes, *in* Porcelli, D., Ballentine, C.J., and Wieler, R., eds., Noble Gases in Geochemistry and Cosmochemistry: Reviews in Mineralogy and Geochemistry 47: Washington, D.C., Geochemical Society and Mineralogical Society of America, p. 731–784, https://doi.org/10.1515/9781501509056-018.

Niemi, N.A., Oskin, M., Burbank, D.W., Heimsath, A.M., and Gabet, E.J., 2005, Effects of bedrock landsliding on cosmogenically determined erosion rates: Earth and Planetary Science Letters, v. 237, p. 480–498, https://doi.org/10.1016/j.epsl.2005.07.009.

Nilius, N.-P., Glotzbach, C., Wölfler, A., Hampel, A., Dunkl, I., Akal, C., Heineke, C., and Hetzel, R., 2019, Exhumation history of the Aydın range and the role of the Büyük Menderes detachment system during divergent extension of the central Menderes Massif, western Turkey: Journal of the Geological Society of London, https://doi.org/10.1144/jgs2018-162.

Nishiizumi, K., Imamura, M., Caffee, M.W., Southon, J.R., Finkel, R.C., and McAninch, J., 2007, Absolute calibration of ^{10}Be AMS standards: Nuclear Instruments & Methods in Physics Research. Section B, Beam Interactions with Materials and Atoms, v. 258, no. 2, p. 403–413, https://doi.org/10.1016/j.nimb.2007.01.297.

Oner, Z., and Dilek, Y., 2011, Supradetachment basin evolution during continental extension: The Aegean province of western Anatolia, Turkey: Geological Society of America Bulletin, v. 123, no. 11/12, p. 2115–2141, https://doi.org/10.1130/B30468.1.

Perron, J.T., and Royden, L., 2013, An integral approach to bedrock river profile analysis: Earth Surface Processes and Landforms, v. 38, p. 570–576, https://doi.org/10.1002/esp.3302.

Perron, J.T., Richardson, P.W., Ferrier, K.L., and Lapôtre, M., 2012, The root of branching river networks: Nature, v. 492, no. 7427, p. 100–103, https://doi.org/10.1038/nature11672.

Portenga, E.W., and Bierman, P.R., 2011, Understanding Earth's eroding surface with ^{10}Be: GSA Today, v. 21, no. 8, p. 4–10, https://doi.org/10.1130/G111A.1.

Prince, P.S., Spotila, J.A., and Henika, W.S., 2011, Stream capture as driver of transient landscape evolution in a tectonically quiescent setting: Geology, v. 39, no. 9, p. 823–826, https://doi.org/10.1130/G32008.1.

Purvis, M., and Robertson, A., 2005, Sedimentation of the Neogene–Recent Alaşehir (Gediz) continental graben system used to test alternative tectonic models for western (Aegean) Turkey: Sedimentary Geology, v. 173, no. 1–4, p. 373–408, https://doi.org/10.1016/j.sedgeo.2003.08.005.

Reilinger, R., McClusky, S., Paradissis, D., Ergintav, S., and Vernant, P., 2010, Geodetic constraints on the tectonic evolution of the Aegean region and strain accumulation along the Hellenic subduction zone: Tectonophysics, v. 488, no. 1–4, p. 22–30, https://doi.org/10.1016/j.tecto.2009.05.027.

Reinhardt, L.J., Dempster, T.J., Shroder, J.F., and Persano, C., 2007a, Tectonic denudation and topographic development in the Spanish Sierra Nevada: Tectonics, v. 26, TC3001, https://doi.org/10.1029/2006TC001954.

Reinhardt, L.J., Hoey, T.B., Barrows, T.T., Dempster, T.J., Bishop, P., and Fifield, L.K., 2007b, Interpreting erosion rates from cosmogenic radionuclide concentrations measured in rapidly eroding terrain: Earth Surface Processes and Landforms, v. 32, p. 390–406, https://doi.org/10.1002/esp.1415.

Ring, U., Brandon, M.T., Lister, G.S., and Willett, S.D., 1999, Exhumation processes, *in* Ring, U., Brandon, M.T., Lister, G.S., and Willett, S.D., eds., Exhumation Processes: Normal Faulting, Ductile Flow, and Erosion: Geological Society of London Special Publication 154, p. 1–27.

Ring, U., Johnson, C., Hetzel, R., and Gessner, K., 2003, Tectonic denudation of a Late Cretaceous–Tertiary collisional belt: Regionally symmetric cooling patterns and their relation to extensional faults in the Anatolide belt of western Turkey: Geological Magazine, v. 140, no. 4, p. 421–441, https://doi.org/10.1017/S0016756803007878.

Roda-Boluda, D.C., D'Arcy, M., Whittaker, A.C., Gheorghiu, D.M., and Rodés, Á., 2019, ^{10}Be erosion rates controlled by transient response to normal faulting through incision and landsliding: Earth and Planetary Science Letters, v. 507, p. 140–153, https://doi.org/10.1016/j.epsl.2018.11.032.

Rojay, B., Toprak, V., Demirci, C., and Süzen, L., 2005, Plio-quaternary evolution of the Küçük Menderes graben southwestern Anatolia, Turkey: Geodinamica Acta, v. 18, no. 3–4, p. 317–331, https://doi.org/10.3166/ga.18.317-331.

Rossi, M.W., Quigley, M.C., Fletcher, J.M., Whipple, K.X., Díaz-Torres, J.J., Seiler, C., Fifield, K.L., and Heimsath, A.M., 2017, Along-strike variation in catchment morphology and cosmogenic denudation rates reveal the pattern and history of footwall uplift, Main Gulf Escarpment, Baja California: Geological Society of America Bulletin, v. 129, p. 837–854, https://doi.org/10.1130/B31373.1.

Schwanghart, W., and Scherler, D., 2014, TopoToolbox 2—MATLAB-based software for topographic analysis and modeling in Earth surface sciences: Earth Surface Dynamics, v. 2, p. 1–7, https://doi.org/10.5194/esurf-2-1-2014.

Şengör, A.M.C., Satır, M., and Akkök, R., 1984, Timing of tectonic events in the Menderes Massif, western Turkey: Implications for tectonic evolution and evidence for Pan-African basement in Turkey: Tectonics, v. 3, no. 7, p. 693–707, https://doi.org/10.1029/TC003i007p00693.

Seyitoğlu, G., and Scott, B.C., 1991, Late Cenozoic crustal extension and basin formation in west Turkey: Geological Magazine, v. 128, no. 2, p. 155–166, https://doi.org/10.1017/S0016756800018343.

Sklar, L.S., and Dietrich, W.E., 1998, River longitudinal profiles and bedrock incision models: Stream power and the influence of sediment supply, *in* Tinkler, K., and Wohl, E.E., eds., Rivers over Rock: Fluvial Processes in Bedrock Channels: American Geophysical Union, Geophysical Monograph 107, p. 237–260, https://doi.org/10.1029/GM107p0237.

Small, E.E., Anderson, R.S., Repka, J.L., and Finkel, R., 1997, Erosion rates of alpine bedrock summit surfaces deduced from in situ ^{10}Be and ^{26}Al: Earth and Planetary Science Letters, v. 150, no. 3–4, p. 413–425, https://doi.org/10.1016/S0012-821X(97)00092-7.

Small, E.E., Anderson, R.S., and Hancock, G.S., 1999, Estimates of the rate of regolith production using ^{10}Be and ^{26}Al from an alpine hillslope: Geomorphology, v. 27, no. 1–2, p. 131–150, https://doi.org/10.1016/S0169-555X(98)00094-4.

Snyder, N., Whipple, K.X., Tucker, G., and Merritts, D.J., 2000, Landscape response to tectonic forcing: Digital elevation model analysis of stream profiles in the Mendocino triple junction region, northern California: Geological Society of America Bulletin, v. 112, no. 8, p. 1250–1263, https://doi.org/10.1130/0016-7606(2000)112<1250:LRTTFD>2.0.CO;2.

Stock, G.M., Frankel, K.L., Ehlers, T.A., Schaller, M., Briggs, S.M., and Finkel, R.C., 2009, Spatial and temporal variations in denudation of the Wasatch Mountains, Utah, USA: Lithosphere, v. 1, p. 34–40, https://doi.org/10.1130/L15.1.

Stock, J., and Dietrich, W.E., 2003, Valley incision by debris flows: Evidence of a topographic signature: Water Resources Research, v. 39, no. 4, 1089, https://doi.org/10.1029/2001WR001057.

Stone, J.O., 2000, Air pressure and cosmogenic isotope production: Journal of Geophysical Research. Solid Earth, v. 105, p. 23,753–23,759, https://doi.org/10.1029/2000JB900181.

Strobl, M., Hetzel, R., Niedermann, S., Ding, L., and Zhang, L., 2012, Landscape evolution of a bedrock peneplain on the southern Tibetan Plateau revealed by *in situ*-produced cosmogenic ^{10}Be and ^{21}Ne: Geomorphology, v. 153–154, p. 192–204, https://doi.org/10.1016/j.geomorph.2012.02.024.

Süzen, M.L., Toprak, V., and Rojay, B., 2006, High-altitude Plio-Quaternary fluvial deposits and their implication on the tilt of a horst, western Anatolia, Turkey: Geomorphology, v. 74, p. 80–99, https://doi.org/10.1016/j.geomorph.2005.07.012.

Thomson, S.N., and Ring, U., 2006, Thermochronologic evaluation of postcollision extension in the Anatolide orogen, western Turkey: Tectonics, v. 25, no. 3, TC3005, https://doi.org/10.1029/2005TC001833.

van Hinsbergen, D.J., Kaymakci, N., Spakman, W., and Torsvik, T.H., 2010, Reconciling the geological history of western Turkey with plate circuits and mantle tomography: Earth and Planetary Science Letters, v. 297, no. 3, p. 674–686, https://doi.org/10.1016/j.epsl.2010.07.024.

von Blanckenburg, F., 2006, The control mechanisms of erosion and weathering at basin scale from cosmogenic nuclides in river sediment: Earth and Planetary Science Letters, v. 242, no. 3, p. 224–239, https://doi.org/10.1016/j.epsl.2005.11.017.

Whipple, K.X., Forte, A.M., DiBiase, R.A., Gasparini, N.M., and Ouimet, W.B., 2017, Timescales of landscape response to divide migration and drainage capture: Implications for the role of divide mobility in landscape evolution: Journal of Geophysical Research. Earth Surface, v. 122, p. 248–273, https://doi.org/10.1002/2016JF003973.

Willett, S.D., Hovius, N., Brandon, M.T., and Fisher, D.M., 2006, Introduction, *in* Willett, S.D., Hovius, N., Brandon, M.T., and Fisher, D.M., eds., Tectonics, Climate and Landscape Evolution: Geological Society of America Special Paper 398, p. 7–11, https://doi.org/10.1130/2006.2398(00).

Willett, S.D., McCoy, S.W., Perron, J.T., Goren, L., and Chen, C.-Y., 2014, Dynamic reorganization of river basins: Science, v. 343, no. 6175, https://doi.org/10.1126/science.1248765.

Wobus, C., Whipple, K.X., Kirby, E., Snyder, N., Johnson, J., Spyropolou, K., Crosby, B., and Sheehan, D., 2006, Tectonics from topography: Procedures, promise, and pitfalls, *in* Willett, S.D., Hovius, N., Brandon, M.T., and Fisher, D.M., eds., Tectonics, Climate, and Landscape Evolution: Geological Society of America Special Paper 398, p. 55–74, https://doi.org/10.1130/2006.2398(04).

Wolff, R., Hetzel, R., and Strobl, M., 2018, Quantifying river incision into low-relief surfaces using local and catchment-wide ^{10}Be denudation rates: Earth Surface Processes and Landforms, v. 43, p. 2327–2341, https://doi.org/10.1002/esp.4394.

Wölfler, A., Glotzbach, C., Heineke, C., Nilius, N.-P., Hetzel, R., Hampel, A., Akal, C., Dunkl, I., and Christl, M., 2017, Late Cenozoic cooling history of the central Menderes Massif: Timing of the Büyük Menderes detachment and the relative contribution of normal faulting and erosion to rock exhumation: Tectonophysics, v. 717, p. 585–598, https://doi.org/10.1016/j.tecto.2017.07.004.

Yılmaz, Y., Genç, S.C., Gürer, F., Bozcu, M., Yılmaz, K., Karacık, Z., Altunkaynak, S., and Emlas, A., 2000, When did the western Anatolian grabens begin to develop?, *in* Bozkurt, E., Winchester, J.A., and Piper, J.D.A., eds., Tectonics and Magmatism in Turkey and Surrounding Regions: Geological Society of London Special Publication 173, p. 353–384, https://doi.org/10.1144/GSL.SP.2000.173.01.17.